Eindhoven University of Technology

MASTER

Are droplet-impact and laser-ablation splashing commutable?

Hermens, Jaap C.J.

Award date:
2020

[Link to publication](#)

Disclaimer
This document contains a student thesis (bachelor's or master's), as authored by a student at Eindhoven University of Technology. Student theses are made available in the TU/e repository upon obtaining the required degree. The grade received is not published on the document as presented in the repository. The required complexity or quality of research of student theses may vary by program, and the required minimum study period may vary in duration.

General rights
Copyright and moral rights for the publications made accessible in the public portal are retained by the authors and/or other copyright owners and it is a condition of accessing publications that users recognise and abide by the legal requirements associated with these rights.

- Users may download and print one copy of any publication from the public portal for the purpose of private study or research.
- You may not further distribute the material or use it for any profit-making activity or commercial gain

Take down policy
If you believe that this document breaches copyright please contact us providing details, and we will remove access to the work immediately and investigate your claim.

Download date: 12. Sep. 2025

Graduation Project

Are Droplet-Impact and Laser-Ablation Splashing Commutable?

Supervised by dr. P. Rindt, dr. O. Versolato, dr. J. Beckers & prof. dr. N. Lopes Cardozo

J.C.J. (Jaap) Hermens 0887890

May 11, 2020

Abstract

In nanolithography industry, extreme ultraviolet (EUV) light sources are used for semiconductor device fabrication. This EUV source is based on laser ablating liquid tin to create a plasma that emits the required 13.5 nm wavelength light. In current day nanolithography devices, a train of tin droplets is ablated with high frequency limited by the droplet dispenser. An alternative concept for an EUV source is investigated, where this limiting droplet dispenser is absent.

In this research, a new EUV source concept derived from nuclear fusion engineering is adopted: a liquid tin film on top of a tungsten substrate. In nuclear fusion reactors, liquid metal films are considered as heat shields. This study focuses on the fluid dynamics after laser impact on a liquid tin film. In the measured laser energy regime, splashing is observed; a crown forms and droplets detach from the crown rim. This splashing is undesirable in an EUV source, where contamination, in the form of ejected droplets, has to be minimized. In addition, during local and temporal heat fluxes in nuclear fusion reactors on liquid metal heat shields (called divertors) droplets could also be ejected, and disturb reactor operation. Thus, there is a joint interest in suppressing splashing caused by heat fluxes.

Since there is an abundance of literature on droplet-impact splashing, and virtually no literature on laser ablation splashing, we compare laser-ablation splashing to droplet-impact splashing. If the splashing dynamics are found to be comparable, knowledge of droplet-impact splashing can be applied to laser-ablation splashing. This knowledge could eventually contribute to designing an EUV source, and liquid metal divertor concept, that suppresses splashing.

The crown evolution of a laser-ablation splash on a 3 mm thick liquid tin film is studied experimentally using shadowgraphy for laser-impact energies of 2.5-30 mJ, focused to a 66 μm full width half maximum (FWHM) Gaussian spot using 8 ns pulses. The results are compared qualitatively, as well as quantitatively to literature describing droplet-impact splashing. Many similarities are observed, apart from the difference in crown collapse. This difference of crown height evolution at late-time can be attributed to the relative importance of gravity on the different length-scale, expressed by the bond number. To make crown measurements and time dimensionless, an energy-dependent characteristic length scale and velocity are defined. In dimensionless units, early-time evolution of crown width (W^*) of the laser-ablation splash is found to be independent of impact laser energy and follows $W^* - 1 \propto \sqrt{\tau}$. This relation agrees with droplet-impact literature. A linear relation between the crown height (H) and width (W) is measured during the crown growth phase. The collection of these linear relations for various laser energies is found to approximately follow the quadratic relation $H \approx 0.01 + 0.33W^2$.

In conclusion, the dimensionless crown growth of the laser-ablation splash correlates well with the dimensionless crown growth of the droplet-impact splash, both theoretically and empirically. Consequently, within the measured regime, laser ablation and droplet impact are approximately interchangeable, considering the early-time crown evolution of the splash.

Contents

Chapter 1

Introduction

Splashing caused by the impact of liquid raindrops is a common occurrence in nature. In addition, splashing is observed in many applications, e.g. sprinkling irrigation, inkjet printing, and fuel drop impact in internal combustion engines [1, 2]. Figure 1.1a shows this frequently observed splashing phenomenon. Fluid dynamics governing droplet-impact splashing has been studied for at least a century, when Worthington (1908) conducted systematic research on droplet-impact splashing [3]. In the Annual Review of Fluid Mechanics 2006, A.L. Yarin writes: "In spite of its commonness, and more than 100 years of research, the phenomenon is still far from being fully understood and continues to attract physicists, engineers, and mathematicians" [4]. Nevertheless, an extensive body of empirical research has been developed, describing scaling of crown evolution and droplet detachment during droplet-impact splashing [2, 5–21]. An alternative cause of splashing can be solids impacting liquids films, moreover, impact of any kind of mass on to liquid can be the origin of a splash. Something less trivial is splashing caused by a local heat pulse on a liquid film. This situation presents itself in two separate disciplines: nuclear fusion engineering and nanolithography.

In nuclear fusion engineering, divertor technology in tokamaks is one of the critical fields that has to improve for future nuclear fusion devices. These heat shields have to withstand millisecond heat pulses up to ~80 GW/m^2, caused by plasma disruptions [22, 23]. There are no solid materials up for that task. For that reason designs using liquid metals, specifically liquid tin [24],

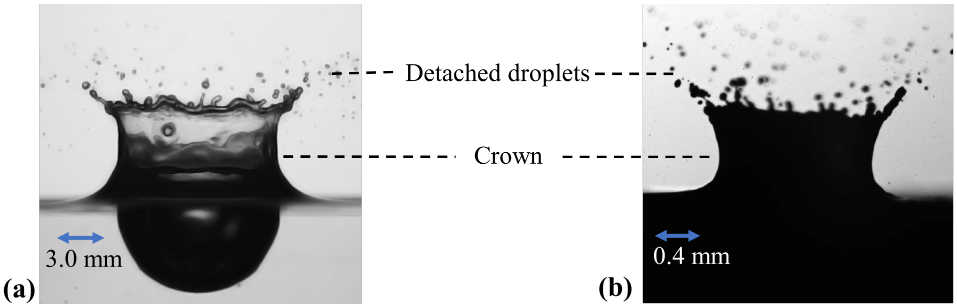

Figure 1.1: (a) Image of droplet-impact splashing in acetic acid 4.9 ms after impact, with a droplet velocity of 4.4 m/s, and droplet diameter of 2.9 mm, figure courtesy of A. Bisighini [7]. (b) Shadowgraphy image of laser-ablation splashing 100 μs after laser impact on liquid tin, with a laser energy of 30 mJ, pulse length of 8 ns (FWHM), and spot size of 66 μm (FWHM).

are being considered [23, 25–27]. Studies have been conducted to analyze splashing of melt layers of solid plasma phasing components. These studies concerned liquid droplet ejection because of intense boiling [28], and splashing caused by the evolution of Kelvin-Helmholtz instabilities at the plasma-liquid interface [29].

Extreme ($\sim 10^8$W), temporal ($\sim$ ns), and local (<1 mm^2) heating is also used in nanolithography industry. In this industry, extreme ultraviolet (EUV) light is used for semiconductor device fabrication. This light, at a wavelength of 13.5 nm, is produced by laser ablating liquid tin to generate a plasma. The highly charged tin ions that are produced in the hot and dense plasma emit an EUV spectrum corresponding primarily to the resonance transitions $4p^6 4d^m - 4p^5 4d^{m+1} + 4d^{m-1} 4f$ in Sn^{8+}-Sn^{14+} [30]. Early in the development of this EUV source, researchers concluded that limiting the mass of the target reduced the formation of debris in the form of target fragments that can cause damage to the device [31]. Therefore, pulsed lasers are used to ablate a falling stream of liquid tin droplets in rapid succession to maximize light output. Over the past years, EUV power output increased to enable high volume manufacturing. Further improvements in EUV light output can be made by using higher power lasers or increasing conversion efficiency [32]. In addition, an increased repetition rate increases EUV power output. Higher repetition rates require an increase in droplet velocity too. However, the droplet velocity is currently already at $\sim$ 100 m/s. In this way, the spacing between consecutive droplets stays constant to prevent radiation coming from the plasma distorting the next droplet. To achieve higher droplet velocities, higher drive gas pressures are necessary. One tries to avoid higher drive gas pressures because it limits the lifetime and reliability of the droplet generator, which is already a limiting component in the system [33]. Hence, other pathways are explored to maximize EUV light production.

This is where both fields of study meet. In this project, a stepping stone towards a new EUV source is investigated: the study of liquid displacement after laser impact on a liquid tin film. This research is relevant for lithography industry because EUV light is generated during laser impact on the liquid tin. In addition, researchers in divertor technology also want to understand the liquid tin behavior after a high-intensity heat pulse. Moreover, both disciplines want to prevent or suppress splashing, to avoid contamination of ejected tin droplets, which are undesirable in both the EUV source and in a nuclear fusion reactor. Preliminary experiments at the Advanced Research Center for Nanolithography Research (ARCNL), found splashing behavior of liquid tin at laser power densities of $> 10^{11}$ W/m^2, using $\sim$ns pulses, as shown in Figure 1.1b. These experiments were conducted on a tungsten 3D- printed liquid metal divertor target designed for fusion research experiments in the linear plasma device Magnum-PSI at the Dutch Institute for Fundamental Energy Research (DIFFER) [23].

Laser ablation of solids has been researched in the past [34–36], and momentum transfer by laser impact on liquid tin droplets has also been studied [37–40]. However, there is no published literature on splashing after laser impact on liquid films. In this report, an introduction into the undiscovered field of laser-ablation splashing dynamics is pursued, to contribute to the end goal of suppressing the laser-ablation splash after liquid metal laser impact. The physics encountered during studying laser-ablation splashing extends across a range of different timescales and different disciplines: optical laser absorption, plasma expansion, and fluid dynamics [41]. Consequently, a theoretical treatment is non-trivial. Therefore, a different approach studying the splashing mechanism after laser impact is chosen; the dynamics of the crown during laser-ablation splashing are compared to the dynamics of the crown during droplet-impact splashing. The goal is to find out if an impacting droplet can be replaced by a laser pulse without changing the crown dynamics. This leads to the following research question:

‘Are droplet-impact splashing and laser-ablation splashing commutable?’

Here, commutability is defined as *‘capable of being substituted, replaced, or interchanged’* [42].

This research question is studied by conducting laser-ablation splashing experiments and tracking the crown evolution with time using stroboscopic shadowgraphy. The analysis focuses on the crown height and width, respectively. Laser-impact energies are varied, and the results are compared to droplet-impact literature. The comparison can be made by using dimensionless parameters widely used in fluid dynamics. In this way, the droplet diameter during droplet impact can be translated to a characteristic length scale in laser impact. Likewise, the droplet impact velocity is translated to laser energy such that droplet impact and laser impact become commutable in the measured regime.

In summary, developing full theoretical understanding of all elements of the laser-ablation splash is challenging. This is due to the complex nature of plasma expansion with high-density laser-produced plasmas as well as complex mechanisms that drive the splashing. However, the considerable amount of research done on droplet-impact splashing presents an opportunity for a comparability study, because both phenomena look alike. This similarity is visible in Figure 1.1. We can experimentally study the laser-ablation splash and compare the dynamics discovered with literature on droplet-impact splashing, e.g., crown evolution with time and droplet detachment. In case of similar dynamics, we can explore which set of parameters for laser impact results in a splash that can also be caused by droplet impact. In this way, the unexplored field of laser-ablation splashing can benefit from the century of research invested in droplet-impact splashing. Ultimately, understanding of the physics driving the laser-ablation splash can contribute to the suppression of debris in the form of target fragments after laser impact. This could make an EUV target without limiting the mass viable, circumventing some of the current limitations in EUV light production. Furthermore, it might be possible to optimize liquid metal divertor designs to suppress droplet ejection during pulsed heat loads.

In Chapter 2, the relevant background concerning droplet impact and laser-matter interaction is presented. Chapter 3 discusses the experimental set-up to measure laser ablation crown evolution over time, including important design steps and an explanation of the written data processing software. In Chapter 4, the results are presented and compared to a droplet-impact splash both qualitatively and quantitatively. In addition, scaling relations are found and discussed. Chapter 5 critically reviews the results in the form of a discussion. Assumptions made during the project are reconsidered and critically weighed. In Chapter 6 a summary and outlook are presented. Chapter 7 outlines the conclusions of this thesis.

Chapter 2

Theory

In this chapter, the physics necessary to describe droplet-impact splashing is discussed. Additionally, an introduction to laser-matter interaction is given.

2.1 Droplet-impact splash

For this project, we focus on perpendicular droplet-impact on liquid. This kind of impact may result in crown formation and breakup depending on impact velocity, drop size, fluid properties, and, in the case of thin films, also roughness and wettability of the solid surface underneath [4]. As schematically illustrated in Figure 2.1, the crown forms in the following chronological order:

1. The impactor induces an initial pressure field.
2. The liquid is set in motion.
3. The surface energy is increased since it is energetically more favorable than increasing the kinetic energy of mass at rest.
4. Liquid leaves the surface and forms a crown.

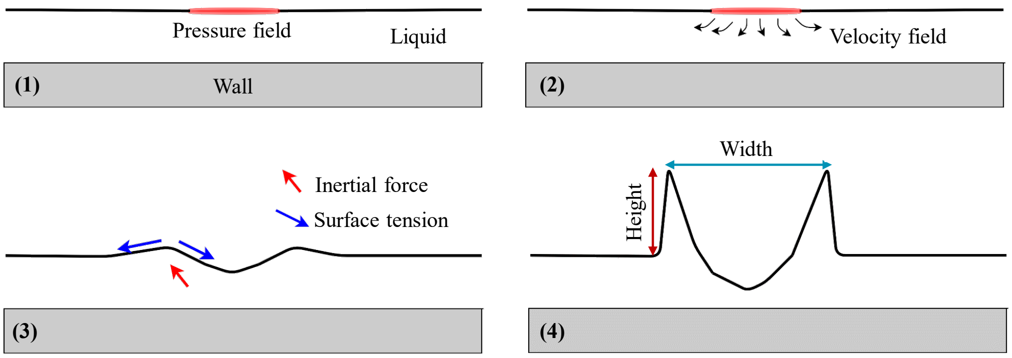

Figure 2.1: Schematic illustration of the crown formation process. The numbers 1-4 match the items in the enumeration.

The shape and magnitude of the induced pressure field, in combination with the fluid properties, fully govern the shape and size of the crown over time. However, a full theoretical model describing this crown growth does not exist [4, 7, 43–45]. Nevertheless, theorists and experimentalists use dimensionless numbers to classify the empirical research done on this subject. The main dimensionless numbers governing crown evolution are the Weber number, Reynolds number, Ohnesorge number, and Bond number:

$$We = \frac{\rho D U^2}{\sigma}, \quad Re = \frac{\rho D U}{\mu}, \quad Oh = \frac{We^{1/2}}{Re}, \quad Bo = \frac{\rho g D^2}{\sigma}, \tag{2.1a-d}$$

with ρ the density, μ the viscosity, σ the surface tension of the liquid, and g the gravitational constant. D is defined as the drop diameter and U the drop impact velocity. These dimensionless numbers connect the relative importance of the inertia, surface tension, viscosity, and gravity. If one of these numbers is much larger or smaller than unity, this means that one or more of these governing quantities is dominant. As a result, the Weber number compares inertia to surface tension; the Reynolds number compares inertia to viscosity effects; the Ohnesorge number compares viscosity to inertia and surface tension, and the Bond number compares gravity to surface tension [4].

2.1.1 Dimensionless parameters

A distinction can be made between two different relevant timescales: the inertial time, and the capillary time. These can be written as

$$\tau_i = \frac{D}{U}, \quad \tau_c = \sqrt{\frac{\rho R^3}{\sigma}}, \tag{2.2a-b}$$

with R the radius of the impacting droplet. Here, the inertial time is the period it takes for the droplet to fully enter the liquid, and the capillary time is the timescale on which capillary action becomes relevant [46]. In droplet-impact literature the time axis is generally made dimensionless through division by the inertial time as $\tau = t/\tau_i$. Furthermore, also the measured length scales are made dimensionless by dividing by the droplet diameter. This results in the dimensionless height and width of the crown, together with the dimensionless film thickness:

$$H^* = \frac{H}{D}, \quad W^* = \frac{W}{D}, \quad h^* = \frac{h}{D}. \tag{2.3a-c}$$

By using the dimensionless parameters introduced in this section, the height and width over time can be analyzed in a fully dimensionless manner. This way, crown evolution of splashes with sets of different starting parameters can be compared [5, 6, 8, 47]. Note that adjustments have to be made to translate these definitions for dimensionless parameters to a laser-ablation induced crown. This translation to laser impact is further elaborated in Section 3.3.

2.1.2 Mathematical description

Yarin and Weiss (1995) developed a theoretical model based on mass conservation and momenta conservation to describe the dimensionless crown growth after perpendicular drop impact onto a thin liquid film [5]. In the paper, a quasi-one-dimensional approach is used, averaging the flow velocity to describe the crown formation for a thin film droplet-impact. This theory is generalized to the two-dimensional plane case by Roisman et al. [47]. The continuity equation of the film is given as

$$\frac{\partial h}{\partial t} + \nabla \cdot (hV) = 0. \tag{2.4}$$

Here, h the layer thickness, t the time, and V the average velocity over the film thickness parallel to the wall.

In the momentum equation, the inertial forces are balanced with the surface tension forces as

$$\rho(\frac{\partial hV}{\partial t} + \nabla \cdot hV^2) = -\nabla(hp_\sigma) + p_\sigma \nabla h, \tag{2.5}$$

where ρ is the density and p_α the capillary pressure. These equations are solved for the velocity of the crown position in the high Weber number regime, which means that the surface tension is negligible. From the velocity of the crown position over time, the position can be found by integrating over time. This width evolution over time follows

$$W^* = C_W(\tau - \tau_0)^{1/2}, \tag{2.6}$$

with τ_0 time of impact and τ=t/τ_i. The analytical expression of C_W for thin-film impact is $\frac{2}{3}\frac{1}{h^{*\frac{1}{4}}}$ based on volume balancing the drop volume and cylindrical impact zone in thin films [48]. However, by using this definition, a systematic overestimation of W^* is found compared to experiments [5]. The overestimation is attributed to neglecting viscous losses in the analytical derivation [5, 47]. Therefore, Yarin and Weiss (1995) use C_W as a fitting parameter [5]. Moreover, in deep pool impact, the impact crater is hemispherical, not cylindrical. In addition, viscous losses are expected to be more significant, resulting in the expression of C_W to be abandoned for $h* > 1$[19]. Nevertheless, the square root relation with C_W as fitting parameter is experimentally tested and valid for $\tau \leq 15$ [5, 6, 21]. Furthermore, there is evidence for a linear relation between W and H in the initial phase of the crown growth, but no explicit relation for H over time is presented [5].

2.2 Laser-matter interaction

In the previous section, the droplet-impact splash was discussed. This splash is set in motion by a pressure field caused by an impactor. For this research project, the droplet is replaced by a ∼ns laser pulse. The laser pulse heats the surface. For metallic targets, the light is absorbed by electrons of the conduction band. The electrons are heated within a picosecond. Next, electron-phonon coupling transfers energy to the metal lattice within several picoseconds [49]. The low thermal diffusivity during the nanosecond pulse length results in an equal thickness between the penetration depth of the laser light and the thickness of the heated layer (∼ 10 nm) [50].

The heating of the liquid metal leads to a phase transition to the gas phase. Most laser energy is absorbed by free electrons that ionize neutral vapor atoms, which lead to a liquid metal plasma. The primary plasma heating mechanism is inverse bremsstrahlung [51]. The vaporization and rapid heating of the plasma leads to a sharp pressure gradient. This pressure gradient drives the plasma expansion [49]. The resulting pressure impulse applied to the target by the expanding plasma has been studied on flat solids as well as spherical liquid droplets [39, 52].

Philips et al. (1988) found the impulse exerted with laser-ablation on solids to follow

$$J_s = A_s \cdot P \cdot t_p = A_s \cdot B_m I^{a_s} \lambda^{b_s} t_p^{c_s}. \tag{2.7}$$

With A_s the laser-spot area, P the pressure exerted on the target, t_p the pulse length. Moreover, I gives the laser intensity, λ the laser wavelength, and B_m a pre-factor dependent on material of impact [53]. For a solid flat target the exponents are determined to be $a_s = 0.7$, $b_s = -0.3$, and $c_s = 0.85$. The relation for the pressure P in equation 2.7 is tested for laser impact on spherical tin droplets by Kurilovich et al. (2016) [38]. A deviation is found in the exponents, that is attributed to the change from planar to spherical target. Substituting the pressure found by Kurilovich et al. (2016) in Equation 2.7 for laser impact on droplet results in exponents $a_d = 0.56$, $b_d = -0.44$, and $c_d = 0.78$. Moreover, Kurilovich et al. (2018) have shown that this process transfers directed momenta to a laser ablated liquid metal. In their experiments a free falling spherical liquid tin droplet is irradiated by a $\sim$ ns pulse of an infrared laser, the velocity achieved parallel to the incoming laser scales as

$$U = K_U(E - E_0)^{\beta}. \tag{2.8}$$

Here, E is the laser energy on droplet, E_0 the ablation threshold energy, and β a scaling parameter found to be 0.60 ± 0.01 for this spherical target. The pre-factor K_U approximately depends on pulse length and droplet size:

$$K_U \approx 36\left(\frac{25\mu\text{m}}{R_0}\right)^{2.2}\left(\frac{t_p}{10\text{ns}}\right)^{0.4}\text{ms}^{-1}\text{mJ}^{-\beta}, \tag{2.9}$$

with R_0 the droplet radius. This empirical scaling law is plotted in Figure 2.2. In summary, a scaling relation between momentum transfer and laser energy is found [38, 39].

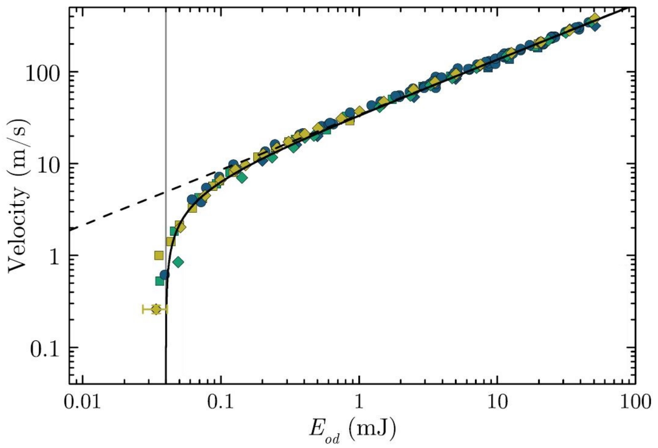

Figure 2.2: Measured propulsion velocity U of liquid tin droplets and tin alloys with a 50 μm diameter after laser impact. The different colours indicate the different droplet composition. Equation 2.8 is plotted as the black solid line. The vertical line corresponds with the threshold energy for droplet propulsion, E_0=0.04 mJ, figure courtesy of D. Kurilovich [39].

Chapter 3

Experimental set-up

In this chapter, the experimental set-up is discussed. The goal of the experiments is to image the laser-ablation splashing phenomena over time, such that the crown height and width (visualized in Figure 3.2 and defined in Figure 3.6) over time can be extracted. First, an overview of the set-up is presented, after which specific elements of the set-up are discussed in more detail.

3.1 Overview

In Figure 3.1, a top view of the experimental set-up is shown. A 1064 nm Nd:YAG laser is guided through a sequence of two thin-film polarizers (TFP) with an adjustable $\lambda/2$ plate in the middle to control laser energy. Thereafter, the beam passes through a beam expander, consisting of a concave lens (f=-150 mm) and a convex lens (f=300 mm) separated by a distance of 45 cm such that the beam size is doubled. After this beam expander an aperture is placed to control the beam size. In the beam tower, the beam is reflected out of the plane of the table upward and back parallel to the table, to increase its height. Next, the beam is led in the vacuum chamber via a convex (f=600 mm) lens and a mirror from the top side. In the chamber, the focused laser spot impacts the target, as shown in Figure 3.2. A H_2 gas inlet to the vacuum chamber realizes an operation pressure of 0.1 mbar. In this pressure regime, the friction of the expanding splash with gas is negligible, and the ratio of oxygen in the operational atmosphere is minimized. In this way, the oxidation of tin and tungsten substrate is decreased [54].

To image the splash as shown in Figure 3.2, a camera and backlight are used. The backlight is a short (5 ns) burst of broadband (560 ± 12) nm light traveling parallel to the target. If the liquid target film deforms, for example, by laser-ablation, the backlight is truncated. In the camera, the light is imaged on a charged-coupled device (CCD). The backlight is generated by focusing a laser pulse in a Rhodamine 6G dye cell that emits the required short burst of light. The light is captured by focusing it on an optical fiber. After that, a combination of curved mirrors creates the collimated light flux aligned with the target and camera. This imaging technique is called shadowgraphy [37–39]. To capture an image of the splash, first, the main YAG laser has to impact the liquid tin to make the film start to deform, after which the backlight pulse is generated and captured by the camera. The shadow of the splash is imaged on the camera. The delay between the laser impact and backlight pulse determines the time step registered. This process is repeated with various time steps to document the splash over time, but only one image can be taken per splash. Consequently, every captured frame comes from a separate and new splash.

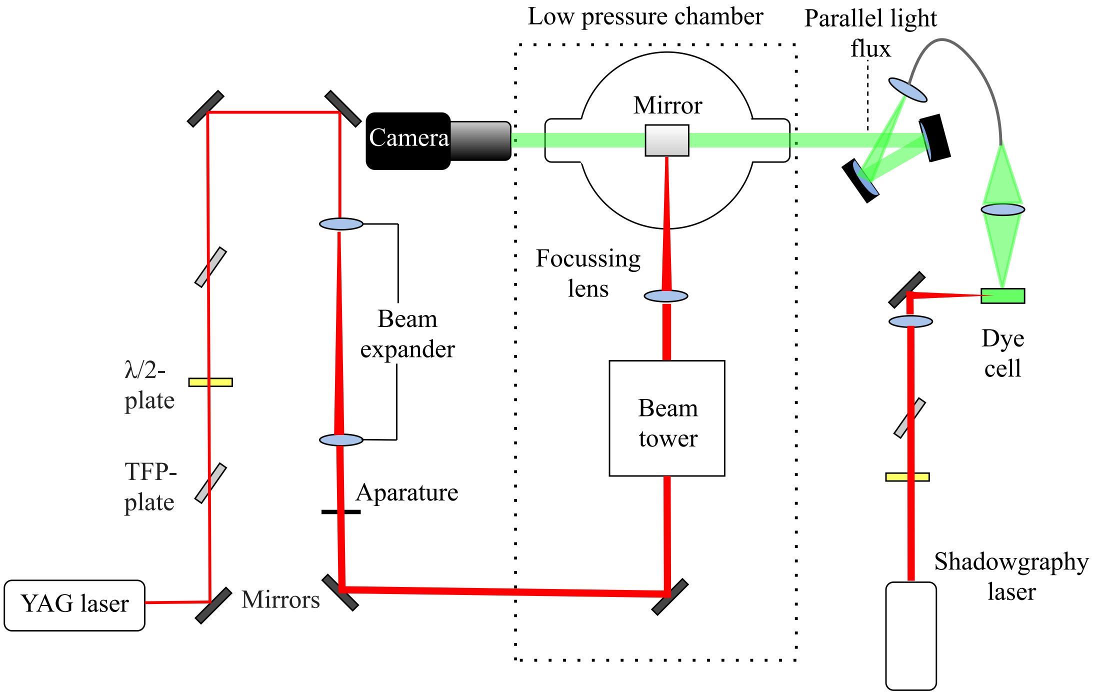

Figure 3.1: Schematical top view of the experimental set-up. The experiment consists of two optical lines. The main laser line is responsible for the laser ablation that starts at the YAG laser. The main laser pulse is guided through a beam-expander to increase beam diameter. Inside the beam tower, the optical line-height is increased. Next, the pulse is focused on the target via the top side window. The laser-ablation splash is imaged stroboscopically using the second optical line. A camera and a backlight are used to image the splash. Figure 3.2 shows a side-view of the low-pressure chamber in which the target is visible.

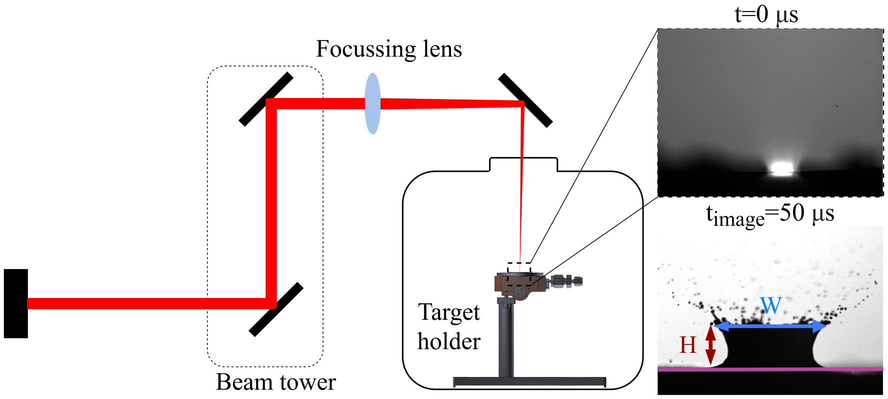

Figure 3.2: Side view of part of the experimental set-up seen in Figure 3.1 indicated by the dotted rectangle. In black, mirrors are depicted. The focused infrared laser impacts the layer of liquid tin on top of the target. The target holder consists of a heater, copper shell, and tungsten substrate with tin on top. Two additional zoomed in figures are added, t_0 showing the plasma light created just after laser-ablation, and t_{image} showing the film deformation after 50 μm.

3.1.1 Laser pulse timing

The triggering of the consecutive main laser, camera, and shadowgraphy laser is crucial to image the splashing phenomenon correctly. The trigger order is schematically shown in Figure 3.3. The camera is triggered 0.9 μs after the main laser to prevent plasma light entering the CCD. Plasma light would locally saturate the image as seen in Figure 3.2, where the trigger order of the camera and main laser is intentionally reversed. The camera is read out 15 ms after the trigger and records all light entering until readout. Light that is not coming from the backlight pulse over this 15 ms period is negligible. Now the delay between the shadowgraphy pulse and main pulse $t_{\mathrm{image,n}}$ determines which time step of the splash is imaged. This triggering process is repeated with a pulse repetition frequency (PRF) of 10 Hz. Accordingly, ten splashes per second are produced, of which ten frames are captured. By adjusting the delay $t_{\mathrm{image,n}}$ in between pulses, the whole crown evolution can be recorded stroboscopically.

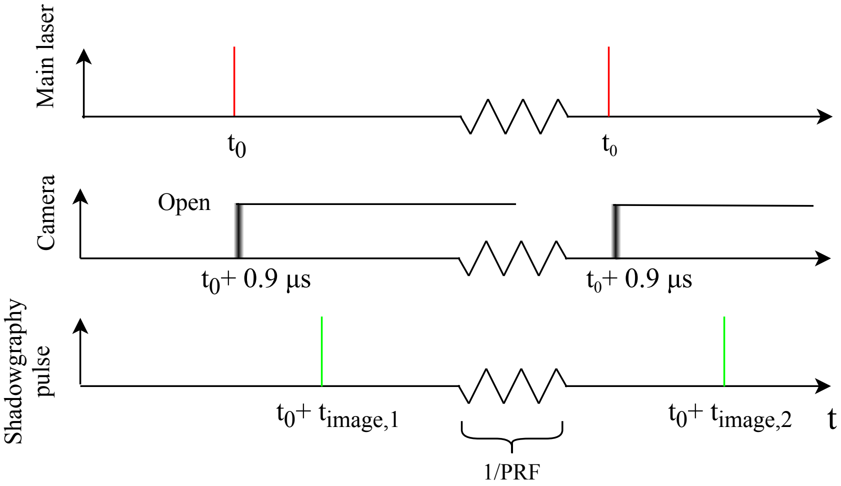

Figure 3.3: Strobstopic imaging order. First, the ablation laser pulse is triggered, shown in red. Second, the camera is opened. Because of the ±0.4 μs jitter of the camera, this is done 0.9 μs after laser impact. Consequently, the plasma light, present until roughly 100 ns after impact, coming from the ablation process is excluded. Third, the shadowgraphy pulse is triggered with a varying delay, $t_{\mathrm{image,n}}$, depicted in green. This process is repeated with a pulse repetition frequency (PRF) of 10 Hz.

3.1.2 Target substrate

A target substrate to hold the liquid tin film was designed and manufactured using 3D printing. Initially, the target is designed for adjustable film thickness, resulting in the target substrate presented in Figure 3.4. Creating a stable thin liquid tin film on top of tungsten could not be accomplished because of wetting problems. The design of the target substrate and wetting problems are further discussed in appendix Section 8.1 and 8.1. We instead use a thick tin layer on the same substrate ($\approx$ 3 mm), of which a top view is seen in Figure 3.4d. The 1 mm pillars are added on the side to calibrate the length scale in shadowgraphy images. To prevent the pillars to be covered with tin, channels are made between the tables and the pillar to separate the pillar from the tin. The tin is originally applied in a vacuum oven at a temperature T>1000 K and pressure P$\sim 10^{-6}$ mbar. During vacuum oven heating, the tin is kept in the center of the target by a ceramic ring. Furthermore, a stop-off pen (tin repellent marker, composition is given in appendix Section 8.2.1), is used around the pillars and in the channels to prevent wetting there. In between experiments, tin is resupplied by adding solid tin at room temperature, which melts when the target is heated to 300 °C. This is the operating temperature and well above the melting point of 232 °C. Moreover, a buffer gas in the form of H_2 is used to minimize oxidation [54].

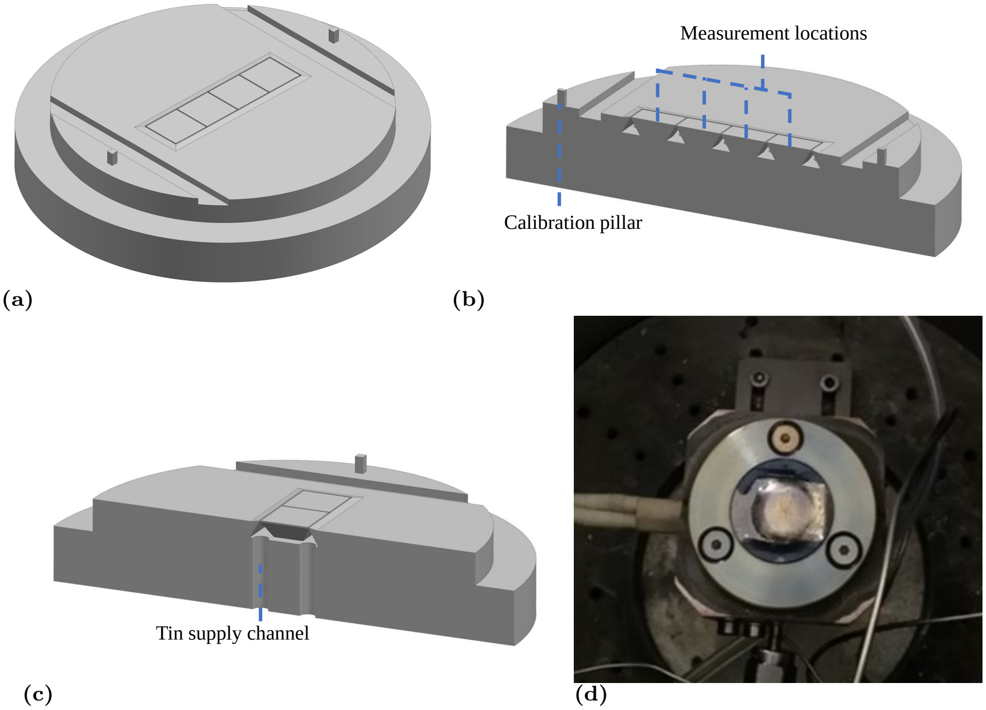

Figure 3.4: Tungsten target design, (a) overview, (b) cross section: the four center islands are the thin-film measurement locations which can be supplied with tin through the bottom channel seen in (c). (d) Top view of loaded target in set-up.

3.1.3 Laser spot size and shape

Equation 3.1 shows the diameter d_0 of the waist of a focused laser:

$$d_0 = 4M^2\frac{\lambda f}{\pi d}. \tag{3.1}$$

Here, M is the beam quality factor, λ is the laser wavelength, f the lens focal length, and d the initial beam diameter [55].

The spot size can be controlled by the aperture in Figure 3.1 because the aperture opening determines d. During the experiments, a Gaussian impact spot size of 66 μm with an ellipticity of (92 ± 2)% is used. Structural constraints precluded the use of a camera inside the chamber. Therefore, before the beam tower, an extra mirror is inserted to divert the beam into a f = 400 mm lens, after which a Complementary Metal Oxide Semiconductor (CMOS) camera is placed. This camera measures the spatial energy profile. The measured profiles are plotted in Figure

3.5. With this specific lens, an average full width half maximum (FWHM) of 50 μm is obtained. This result can be used to calculate the spot size of the f = 600 mm focusing lens used in the laser-ablation experiments. Following Equation 3.1, a minimum spot size with a FWHM of 66 μm is found.

An ideal diffraction-limited beam ($M = 1$) would have a minimum spot size of 51 μm for the given optical system (using f = 600 mm). Thus the beam quality factor is found to be $M = 1.14$. The deviation compared to the diffraction-limited beam can be explained by the numerical aperture of the lens system.

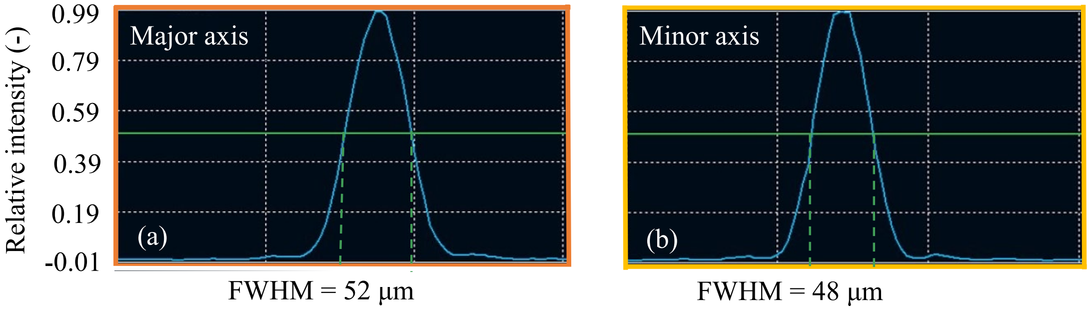

Figure 3.5: Spatial laser profile cross-section in focus (a) major and (b) minor axis. The 2D Gaussian has an average FWHM of 50 μm. This is measured with a CMOS camera placed outside the low-pressure chamber, using a secondary f = 400 mm lens.

3.2 Data processing

In Figure 3.6, the sequence of image analysis operations is shown, which are used to extract the height and width of the crown. The height and top width of the crown from a typical frame (Figure 3.6a) are extracted in the following way. First, a background image is subtracted, which is recorded before impact. The background image contains a frame with the liquid film, but without splash visible. The difference is seen in Figure 3.6b. The obtained difference is binarized, and small white areas (<4000 pixels of a 1388x1038 image) are excluded, removing most droplets, shown in Figure 3.6c. Now the boundary of the splashing area, which encircles the full crown, is tracked. The tracked boundary is plotted in the original image, as shown in Figure 3.6d. The bottom of the splash is chosen by hand for every new measurement series because the grayscale gradient at the tin boundary causes the algorithm to find an inaccurate bottom boundary, as shown by the bottom boundary found in Figure 3.6d. The manually picked bottom boundary is plotted in purple in Figure 3.6e.

The height of the crown is defined as the difference between the bottom of the crown and the rim position, as done in droplet-impact literature [5, 6, 8, 47]. The rim position is found by evaluating the lowest point on the top boundary, which is found by choosing a region of interest (RoI), seen in yellow, and evaluating the minimum vertical coordinate of the tracked boundary as the rim height. A more in-depth explanation of the RoI choice is given in appendix Section 8.5, in addition to the full Matlab code.

The top width is determined by finding the horizontal coordinates where the tracked boundary crosses the previously defined rim height, seen in blue. These locations are marked with red circles. The distance between the two red circles is defined as the top width. This process is repeated for every frame.

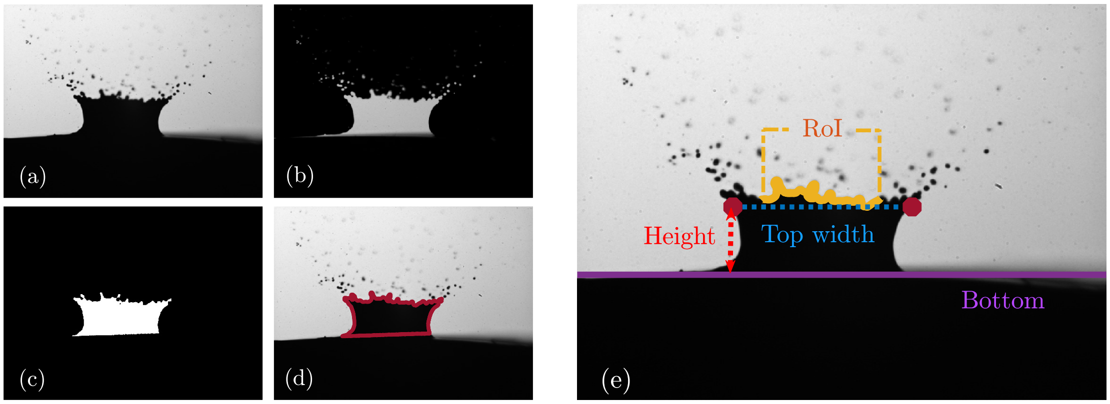

Figure 3.6: Image processing steps to find the height and the top width: Start with (a) grayscale shadowgraphy image of crown, (b) subtracted background, (c) binarized image and small region subtraction, (d) boundary tracking. (e) Finally, a Region of interest (RoI) and bottom of crown are defined, from which the height and top width follow.

It is also desirable to extract and analyze crown angle and bottom width as often done in droplet-impact literature [6, 8]. However, the blur at the bottom edge with the film causes the uncertainty in the bottom width detection to be unacceptably high. Therefore, automated detection is not possible with the current analysis code. The crossing of the bottom boundary with the crown edges can not be obtained in a robust manner, nor can the angle of the crown be calculated.

3.3 Characteristic velocity and length scale

The dimensionless parameters introduced for droplet impact in Section 2.1 can be applied in laser-ablation splashing if we can determine a relevant characteristic velocity and length scale. As an Ansatz, these are chosen to be the first measurable crown velocity and crown diameter.

During early crown expansion (t < 10 μs), when the crown is relatively small, automated height and width detection are not possible with the current analysis code due to the low resolution compared to the crown size. Therefore, these early time steps are analyzed by hand. In Figure 3.7a the crown tip position and bottom width are shown for a typical early-time laser-ablation splash. The crown-tip position over time is plotted in Figure 3.7. The characteristic velocity is defined as the linearly interpolated slope of the crown-top position over time at $(3 < t < 8)$ μs, as presented in Figure 3.7b.

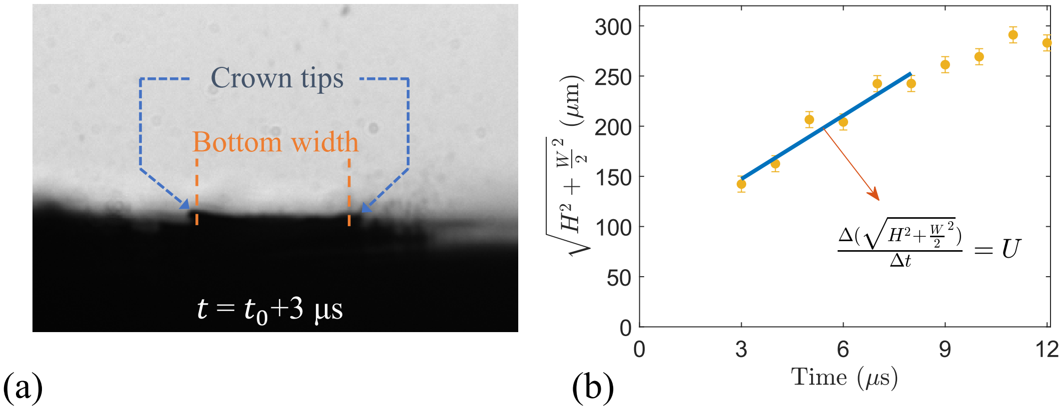

Figure 3.7: (a) Position of manually picked crown tips and bottom width of an example laser-ablation splash. (b) Crown-tip position, with top width (W) and height (H), plotted over time. The initial velocity of the crown is found by linearly fitting over the expansion phase up to 8 μs.

Chapter 4

Results

This chapter presents the results of the conducted experiments, including the scaling of the crown evolution of the laser-ablation splashing phenomena with different laser energies. First, a qualitative comparison to the droplet-impact splash is made in Section 4.1, after which they are quantitatively compared using dimensionless units in Section 4.2. In Section 4.3, a laser energy scan at constant laser spot size is shown. We focus here on early timescales of the crown evolution because these are well described in droplet-impact literature. A detailed analysis of the crown height and top width evolution over time is presented. In Section 4.4, the relation between crown height and crown top width is investigated.

4.1 Qualitative comparison

The results of a droplet-impact experiment conducted by Bisighini (2010) are qualitatively compared with our laser-ablation splashing results [7]. The droplet-impact splash over time is shown in Figure 4.1(a)-(e). The laser-ablation splash over time is shown in Figure 4.1(f)-(j). The droplet-impact experiments were performed in acetic acid, while the laser-ablation experiments are done with liquid tin. The fluid properties of these liquids are given in Table 4.1.

Table 4.1: Fluid properties acetic acid and tin with ρ the density, μ the viscosity, and σ the surface tension [7].

	Fluid	ρ (kg/m^3)	μ (kg/m·s)	σ (N/m)
droplet-impact splash	Acetic acid	1.04x10^3	0.8x10^{-3}	7.12x10^{-2}
laser-ablation splash	Tin	6.99x10^3	1.5x10^{-3}	5.75x10^{-1}

The droplet-impact splash presented here is a deep-pool splash of an oblate droplet impacting at high Weber number. The impact of a more spherical droplet is discussed in Section 5.1. Initially, fast growth of the crown is observed (Figures 4.1a and 4.1b), after which the crown collapses inwards (Figures 4.1c and 4.1d), followed by a jet in the center (Figure 4.1e). We can compare this to a typical laser-ablation splash measured in this project. An order of magnitude difference in length-scale and two orders of magnitude difference in timescale are observed. However, qualitatively the same growth (Figures 4.1f and 4.1g), collapse (Figure 4.1h and 4.1i) and jetting (Figure 4.1j) features are visible. A notable disagreement is the height of the central jet shown in Figures 4.1e and 4.1j. The droplet-impact central jet is significantly larger than

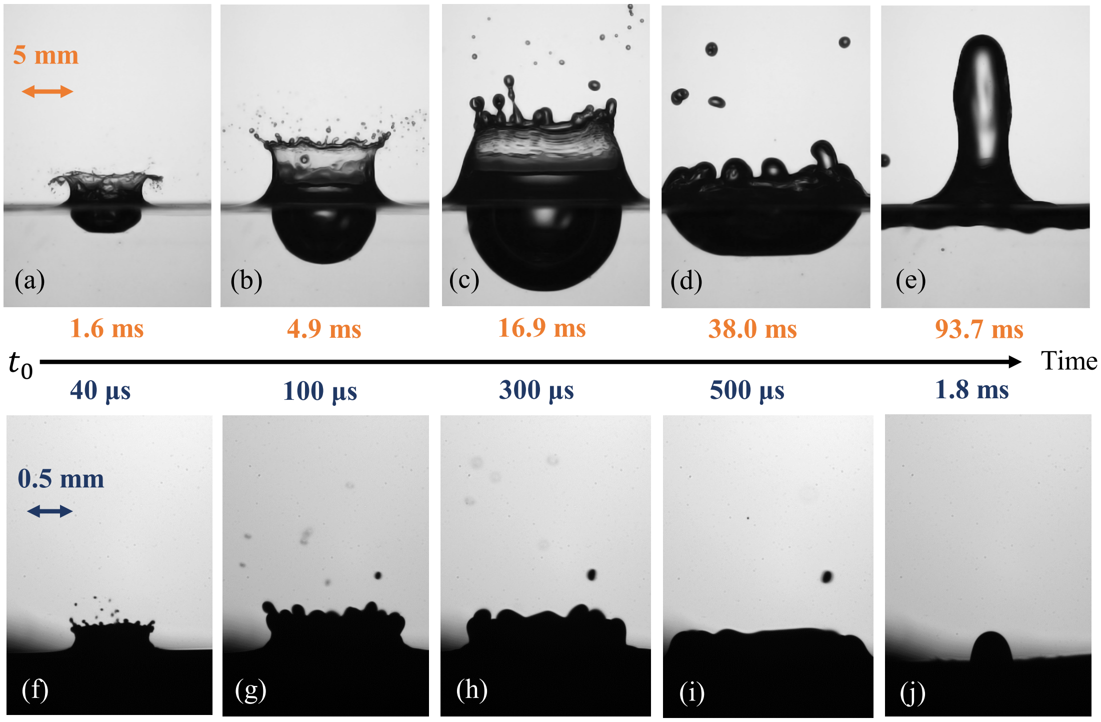

Figure 4.1: (a-e) droplet-impact splashing over time, this splash is the result of an oblate droplet with an average diameter of 2.9 mm and a 15% difference between the major and minor axis, impacting acetic acid with a velocity of 4.4 m/s, figure courtesy of A. Bisighini [7]. (f-j) laser-ablation splashing over time, this splash is the result of an infrared laser pulse with an energy of 10 mJ, a pulse length of 8 ns (FWHM), and a Gaussian spatial pulse shape. t_0 indicates the moment of drop impact and laser-ablation.

the size of the laser-ablation central jet. Castillo Orozco et al. (2015) show how the maximum obtained height of this central jet scales with the Ohnesorge number [9]. In Table 4.2 the relevant dimensionless numbers are compared. The Ohnesorge number is significantly higher for the droplet-impact splash compared to the laser-ablation splash; thus, the central jet of the droplet-impact splash is expected to be larger.

4.2 Quantitative comparison

To compare the crown evolution after droplet impact with the crown evolution after laser ablation, not only the different origins of fluid displacement have to be considered. In addition, the vastly different length scale and timescales of the two phenomena have to be taken into account. This is done in droplet-impact literature using the dimensionless length scale and timescale, as discussed in theory Section 2.1. To transfer to this dimensionless system, the droplet diameter and impact velocity are used to establish a dimensionless length scale and timescale as introduced in Equations 2.2a, 2.3a, and 2.3b. However, during laser ablation there is no droplet, hence no diameter or impact velocity. Therefore, we use the first observable crown width as the characteristic length scale and the first measurable velocity as the characteristic velocity, which are determined as presented in Section 3.3. Now the comparison of these impact parameters

Table 4.2: Impact parameters $D_{D,L}$, $U_{D,L}$, resulting timescales and dimensionless numbers of the presented droplet-impact and laser-ablation splash in Figures 4.1 and 4.2. The inertial time τ_i, capillary time τ_c, and relevant dimensionless numbers are calculated using characteristic length scale $D_{D,L}$ and characteristic velocity $U_{D,L}$. (a)For the laser-ablation splash, length scale D_L and velocity U_L are chosen to be the first observable crown width and first observable crown velocity.

	Droplet-impact splash	Laser-ablation splash
$D_{D,L}$ (m)	2.9x10^{-3}	2.5x10^{-4} (a)
$U_{D,L}$ (m/s)	4.4	28.0 (a)
τ_i (s)	6.6x10^{-4}	1.2x10^{-5}
τ_c (s)	1.1x10^{-2}	1.6x10^{-4}
Weber number	10^3	10^3
Bond number	1	10^{-3}
Reynolds number	10^4	10^4
Ohnesorge number	10^{-2}	10^{-3}

and resulting timescales is presented in Table 4.2.

Using the inertial time to make the time dimensionless ($\tau = t/\tau_i$), and the characteristic length scale to make the length scale dimensionless ($H^*=\frac{H}{D}$, $W^*=\frac{W}{D}$), the two crown phenomena can be compared quantitatively. In Figure 4.2, both the dimensionful as well as the dimensionless height and width evaluations of the laser-ablation crown and droplet-impact crown over time are shown. Introducing dimensionless parameters enables the two phenomena to be compared to one another. They seem to evolve similarly in dimensionless height and width. However, there is a factor two difference in height, and especially at later times ($t > t_c$) also the shape of the height curve starts to differ. The crown after droplet-impact decline accelerates, while the laser-ablation crown declines close to linearly.

Similar behavior over inertial time is demonstrated using the dimensionless time. Consequently, the inertial timescale is a good measure to explain differences in timescale. The capillary time is the timescale on which surface forces become relevant, indicated in Figure 4.2 as the dotted lines. Both capillary times approach the time when the topmost crown height is reached. This is an indication that surface tension is of importance.

Furthermore, the dimensionless numbers introduced in theory Section 2.1 are compared in Table 4.2. Both phenomena take place in the high Weber, high Reynolds, low Ohnesorge regime, hence inertia is dominant and viscous forces are not important. However, there is a discrepancy in the Bond number. The difference in crown decay can be attributed to different forces responsible for the decay. Where the Bond number is in the order of unity for the droplet-impact case, this same dimensionless number is 10^{-3} for the laser-ablation crown. This difference in Bond number means that gravity, as well as surface tension, drive the droplet-impact crown to the surface, while only surface tension is relevant for the crown decline after laser ablation. Moreover, the importance of surface tension highlights the relevance of capillary work and the capillary timescale. The factor two difference in maximum achieved dimensionless height will be further discussed in Section 5.3.2.

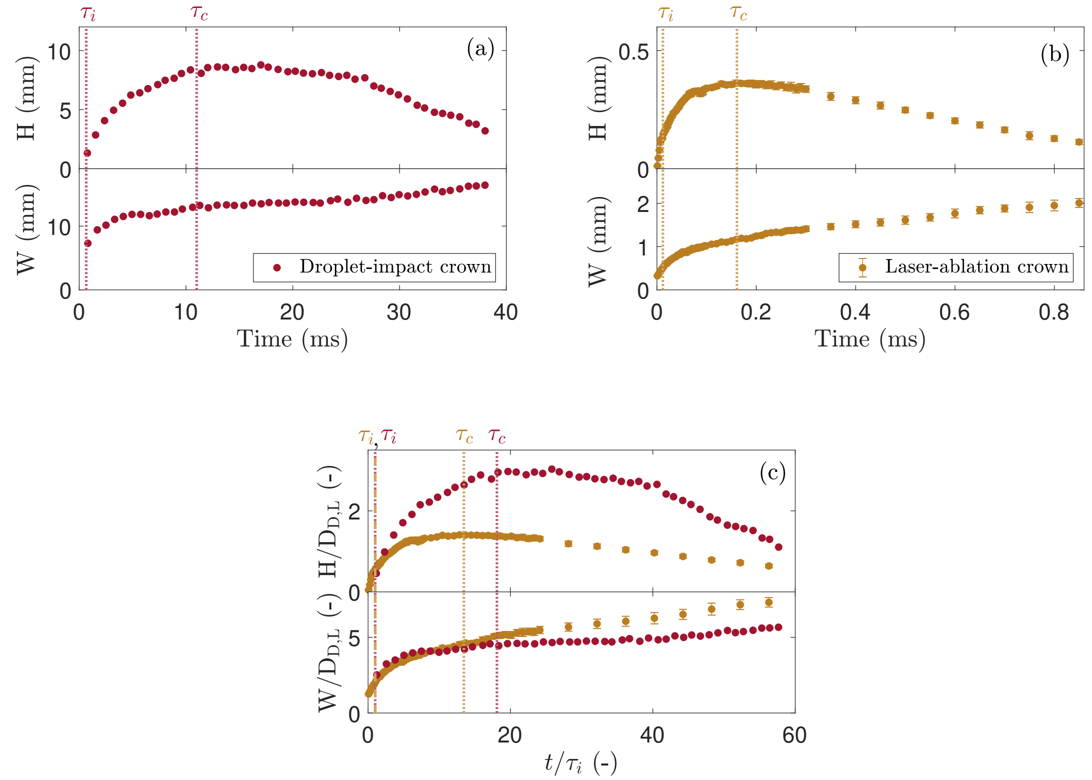

Figure 4.2: Crown evolution over time where (a) corresponds to the droplet-impact splashing images in Figures 4.1(a-e): 2.9 mm droplet impacting acetic acid with 4.4 m/s, and (b) corresponds to laser-ablation splashing images in Figures 4.1(f-j): 10 mJ laser energy impacting liquid tin with a spot size of 66 μm, and pulse length of 8 ns (FWHM) [7]. Height and width are plotted over time. (c) Dimensionless droplet impact and laser ablation combined.

4.3 Laser energy scan

In the previous sections, we made plausible that the droplet-impact and laser-ablation splash behave similarly. To answer the research question: 'Are droplet-impact and laser-ablation splashing commutable?', we have to find interchangeability between the relevant parameters in both phenomena. This is done by first documenting the expansion of the crown of the laser-ablation splash with time for different laser energies.

In figure 4.3, the height and top width of the crown as function of time, using various laser pulse energies, are plotted. Higher energies lead to increased maximum height and a wider crown. The height of the crown exhibits a stronger dependency on laser pulse energy than its width, further discussed in Section 4.4.

The first measurable crown width and crown velocity are extracted for the various laser energies. The results are plotted in Figure 4.4. The first measurable bottom width is extracted at 3 μs after laser ablation. Initial velocity is extracted as explained in Section 3.3. The first measurable width scales weakly and approximately linear with laser energy, following $D_L = (208 \pm 6) + (4.1 \pm 0.4)E$ as is shown in Figure 4.4a. Uncertainties following from fitting procedures are presented as standard deviations; this applies to the entire report. The first measurable velocity increases with energy shown in Figure 4.4b with logarithmic axes.

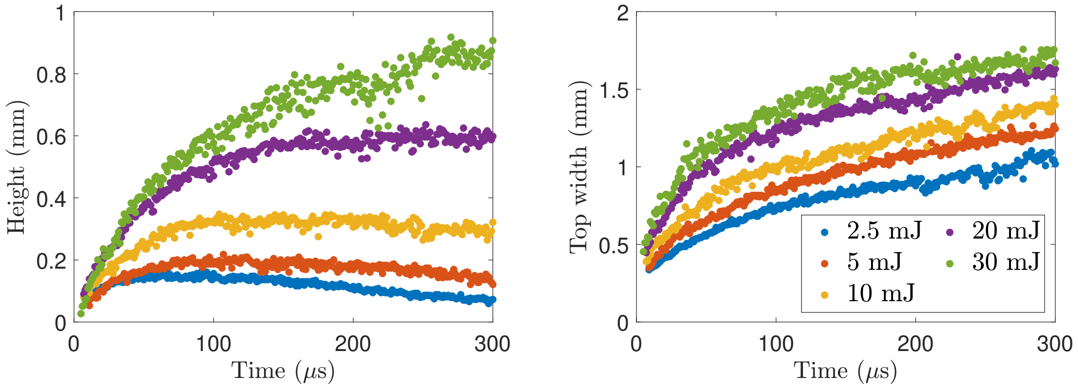

(a) **(b)**

Figure 4.3: Crown evolution over time after laser ablation of liquid tin, using different laser energies. Short laser pulses of 8 ns (FWHM) are focused to an 66 μm FWHM Gaussian spot. Crown height (a) and crown top width (b) over time for laser energies between 2.5 mJ and 30 mJ are plotted.

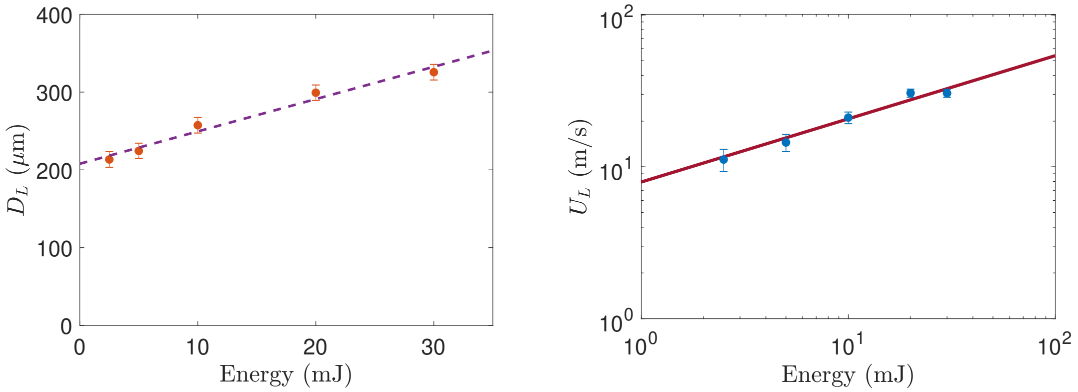

(a) **(b)**

Figure 4.4: The first observable crown width and crown velocity are shown for different laser energies using a constant spot size of 66 μm (FWHM) and a pulse length of 8 ns (FWHM). (a) Presents the approximately linear relation of the characteristic length scale with energy: $D_L = (208 \pm 6) + (4.1 \pm 0.4)E$. (b) shows the power-law (U_L=$K_L E^{\beta_L}$) fit, with $C_1 = 8 \pm 1$ and $C_2 = 0.4 \pm 0.1$, plotted with logarithmic axes.

In equation 2.8, a power-law describing the relation between laser energy and momentum transferred after laser ablation of a spherical liquid metal tin droplet is introduced. The momentum transferred to a droplet in free fall by the plasma, created by laser-impact, is straightforward to measure knowing the mass and velocity of droplet after impact. However, this is less trivial for the laser ablation of a liquid pool. The amount of mass set into motion is unknown; furthermore, the velocity field is more complex [56]. Nevertheless, Duffhues (2020) has shown that the threshold energy E_0 for momentum transfer is negligible at a spot size of 66 μm in the laser energy regime we measured [57]. We use the power-law $U_L = K_L E_L^{\beta}$ with K_L and β_L fitting parameters. Our fitted power $\beta_L = 0.4 \pm 0.1$ differs from literature (using $\beta = 0.60$). Nevertheless, the pre-factor is within the same order of magnitude, $K_L = 8 \pm 1$ compared to $K_U = 36$ $\mathrm{ms}^{-1}\mathrm{mJ}^{-\beta}$. The reason for these discrepancies can be the difference in spatial impact shape; in our case, a full Gaussian pulse impacts the target, whereas in [39] the Gaussian pulse is much wider than the impacted droplet, which thus feels a more homogeneous laser pulse. Moreover, the unknown amount of mass set in motion, likely changing with energy, can also contribute to the discrepancy in fitting parameters.

4.3.1 Width evolution

The previously defined characteristic length scale and velocity are used to make the measurements presented in Figure 4.3b dimensionless. The result is plotted in Figure 4.5a. Measurements for various laser energies collapse onto a single curve, especially up to $t \approx 10\tau_i$. This is expected from droplet-impact literature, introduced in theory Section 2.1.2. However, applying this theoretical relation from droplet-impact literature to the laser-ablation results in Figure 4.5a results in a bad fit. Nevertheless, this could be expected, because the dimensionless crown width in droplet-impact splashing follows the square root law introduced in Equation 2.6, this law crosses the origin: (t=t_0,W^*=0). Moreover, we do not expect the laser-ablation crown width to cross the origin. We hypothesize that in droplet impact there is a moment in time where the interaction region of the droplet is infinitesimal, which is not the case in laser ablation. The Gaussian laser spot interacts with the liquid over the full width of the spot at the same time. It is because of this finite size of the ablating laser spot that we do not expect the width to cross through (0,0). Therefore, to compare the droplet-impact case and laser-ablation case, the width is corrected by subtracting the starting width. This approach is similar to the analysis of disk impact in literature [56]. The initial width subtraction is done in Figure 4.5b.

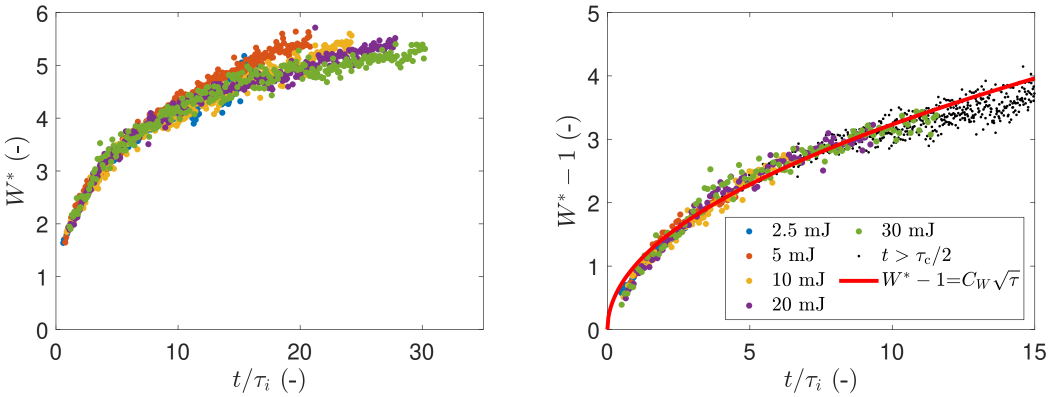

(a) **(b)**

Figure 4.5: Evolution of the crown top width for various energies using a constant spot size of 66 μm (FWHM) and a pulse length of 8 ns (FWHM). (a) Both axis are made dimensionless, after which in (b) the data is shifted downwards by a value of 1 to incorporate starting width. Note the reduced range on the time-axis. Only early time data ($t < \tau_c/2$) is used for the fit $W^* - 1$=$C_W\sqrt{\tau}$. $C_W = 0.96 \pm 0.02$ is found.

Furthermore, the theoretical width evolution over time from droplet-impact literature, introduced in Equation 2.6, is fitted through the initial width expansion phase after subtracting starting width, $W^* - 1 = C_W\sqrt{t/\tau_i}$. Times up to $t = \tau_c/2$ are used to exclude surface tension effects, as differences between droplet-impact and laser-ablation splashing become qualitatively more apparent on the capillary time. Good agreement is found between the dimensionless crown evolution after laser-ablation and the fit that is based on droplet-impact theory. The found value $C_W = 0.96 \pm 0.02$ is not directly analytically interpretable as discussed in theory section 2.1.2 [7].

4.3.2 Height evolution

In this section, all measurements for crown height over time in Figure 4.3a are also made dimensionless using the inertial time from Equation 2.2a for time and Equation 2.3a for height. Figure 4.6 shows the dimensionless height over the dimensionless time. The collapse seen for the dimensionless height is not as good as for the dimensionless top width. From Figure 4.6b, it is clear that the collapse is only seen in very early timescale up to $t \approx 3\tau_i$ (note the difference in plotted range on the horizontal time axis). In addition, there is a small negative offset of the bottom of the crown because of the imperfect bottom crown detection. The limitation of the imaging technique can explain this offset. The crown is imaged parallel to the target surface, if the surface is not perfectly flat, the image is truncated. This is more pronounced close to the surface, meaning the bottom part of the crown is less visible. This poor visibility results in a systematic overestimation of the vertical position of the bottom of the crown.

The square root law from Equation 2.6 is also expected to be valid for the height dependence because of the linear relation between height and width, as discussed in theory section 2.1.2. The square root law over time with the negative height offset, H_0^*, is fitted for the collapsed part of the height evolution: $H^* = H_0^* + C_H\sqrt{\tau}$. The result is plotted in Figure 4.6b.

We can conclude that the square root relation for width evolution with time is valid up to later times ($t = \tau_c/2$) than for the height evolution ($t \approx 3\tau_i$). However, also the pre-factor C_H can be the cause of the short time-span. One can imagine that in all separate laser energy measurements the following relation holds: $H^* \propto \sqrt{\tau}$, but the constant C_H changes in each of these measurements [20]. The following section shows that this is indeed the case.

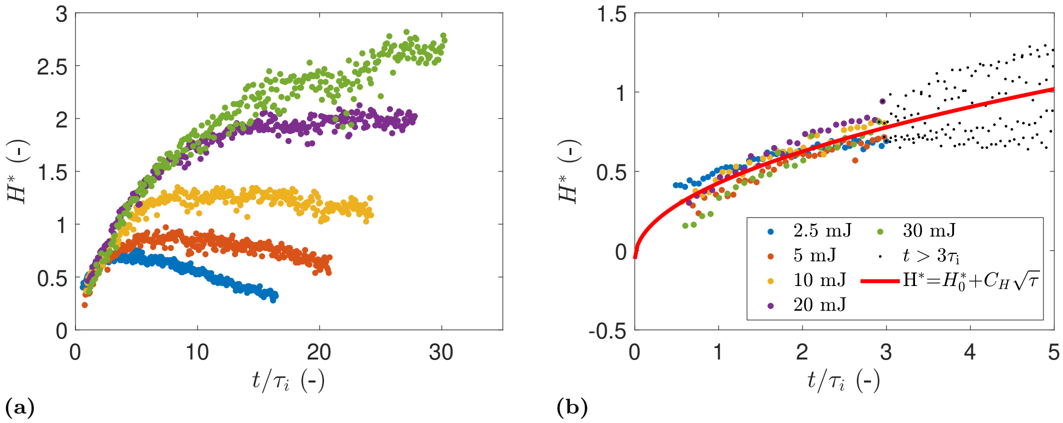

(a) **(b)**

Figure 4.6: Evolution of the crown height for various laser energies using a constant spot size of 66 μm (FWHM) and a pulse length of 8 ns (FWHM). (a) First both axes are made dimensionless after which in (b) the square root law: $H^* = H_0^* + C_H\sqrt{\tau}$ is fitted with $H_0^* = -0.05 \pm 0.06$ and $C_H = 0.49 \pm 0.05$. Note the reduced range on the time-axis. Only early time data ($t < 3\tau_i$) is used for the fit.

4.4 Height versus width analysis

So far, we have evaluated the crown evolution separately, in terms of height and width, of a splash caused by laser ablation of a liquid film over time. We found that the width of the crown evolves over time as $W^* - 1 = C_W\sqrt{\tau}$ for $t < \tau_c/2$ for various laser energies. In addition, the height evolution over time roughly follows $H^* = H_0^* + C_H\sqrt{\tau}$ for $t < 3\tau_i$. However, it is possible that the height evolution over time follows a square root law for various laser energies, but that the constant C_H varies with laser energy [20]. This is investigated by studying the relation between the crown height and crown width over time. As long as a linear relation, $H \propto W$, holds, the time evolution is similar.

In figure 4.7a the height versus width evolution of different laser energies are plotted. The inertial growth phase ($t < \tau_c/2$) is shown in color. The relation between the height and width is mostly linear. This linearity implies that both height and width evolve similarly over time. We previously established a square root law accurately describes the crown width evolution over time, and the linear relation between crown height and width suggests that the crown height also evolves proportionally to $\sqrt{\tau}$.

Another noticeable fact is that the slopes of the height versus width plots differ for different laser energies. Moreover, these slopes differ in such a way that the height versus width results together form an approximately quadratic relation H=0.01+0.33W^2, as visualized in Figure 4.7b, with H_0=0.01 mm. However, every individual laser energy creates a crown where the height and width scale linearly. Thus, this quadratic relation can be seen as $H = C_E(E)W + C_0(E)$ with $C_0(E)$ and $C_H(E)$ energy-dependent constants, such that in the measured range $C_E(E)$ and $C_0(E)$ scale that $H \approx H_0 + C_qW^2$ is obtained for various laser energies, with H_0 the offset height found in Section 4.3.2 and C_q a fitting parameter. However, the lowest measured energy causing splashing, 2.5 mJ, deviates from this relation, clearly shown in Figure 4.7a. This disparity is further analyzed in Section 5.3.2.

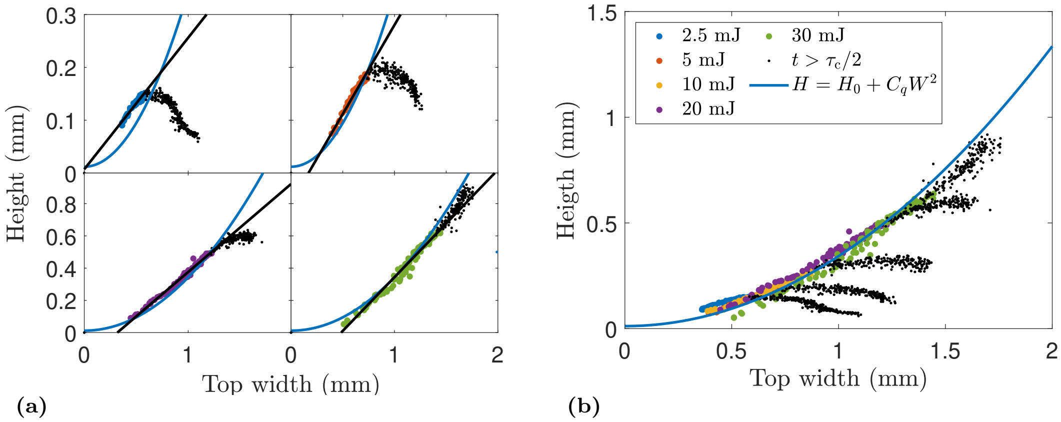

Figure 4.7: Crown height versus width, applying different laser energies using a constant spot size of 66 μm (FWHM) and a pulse length of 8 ns (FWHM). The merge of individual mostly linear relations in the inertial phase ($t < \tau_c/2$) for various laser energies: $H = 0.25W + 0.01$ for 2.5 mJ, $H = 0.34W - 0.06$ for 5 mJ, $H = 0.55W - 0.18$ for 20 mJ, and $H = 0.67W - 0.32$ for 30 mJ shown in (a) results in a quadratic relation (b) fitted using H=$H_0 + C_qW^2$ with offset height $H_0 = 0.01$ mm and C_q=(0.33 ± 0.01) m^{-1}.

This quadratic relation brings our attention back to Section 4.2 of this chapter, where comparable behavior of droplet-impact and laser-ablation splashing is presented. Nonetheless, in Figure 4.1, we found a factor two difference in magnitude of dimensionless height; this is a significant discrepancy. We can now apply the knowledge of the scaling of crown height and width: Recall that the dimensionless width virtually does not dependent on energy (Figure 4.5). However, dimensionless height does (Figure 4.6). Following the relation $H \propto W^2$ that we found for increasing laser energy (Figure 4.7b), we can increase laser energy to recreate Figure 4.2c, with a more appropriate laser energy, such that the droplet-impact splash can be compared better to the laser-ablation splash. In this case, the highest laser energy measured 30 mJ most closely matches measurements from droplet-impact literature. In Figure 4.8 this is shown. Unfortunately, no laser-ablation experiments are capturing this laser energy over the full duration of the splash because of the focus of these experiments laid on the inertial expansion phase. Nevertheless, there is a clear improvement in comparability compared to Figure 4.2c.

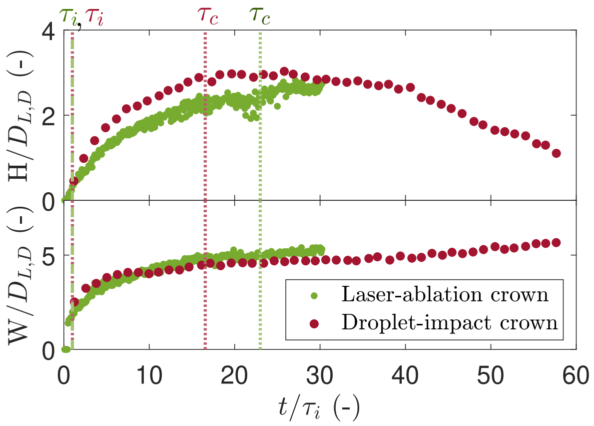

Figure 4.8: Dimensionless height and width of droplet-impact splashing over time, of a 2.9 mm diameter droplet impacting acetic acid with 4.4 m/s seen in red [7]. Laser-ablation splashing is shown in green. A laser energy of 30 mJ with a spot size of 66 μm (FWHM), and a pulse length of 8 ns (FWHM) is used. The vertical lines in red plot the relevant timescales of the droplet-impact splash, in green the timescales of the laser-ablation splash are shown.

Chapter 5

Analysis

In this chapter, the results are further analysed and discussed. The assumptions that have been made are evaluated. The topics presented in Chapter 4 are discussed separately.

5.1 Qualitative comparison analysis

in Section 4.1, the results of the qualitative comparison, laser-ablation of liquid tin with a 66 μm FWHM Gaussian spot size, 10 mJ laser energy, and 8 ns pulse length (FWHM) is compared to acetic acid deep-pool droplet-impact with a 2.9 mm diameter, and droplet-impact velocity of 4.4 m/s. Both crown evolution's show similar features: growth, collapse, and jetting. An absent feature is bubble formation, frequently observed after droplet impacts into a deep pool [7, 8, 17, 58]. Bisighini (2010) studied droplet-impact splashing and found that the inclination of the crown over time was heavily dependent on droplet shape. Moreover, in Figure 5.1, splashes resulting from an oblate-droplet impact and more spherical droplet impact are presented.

Figures 5.1(a)-(e) show the splash produced by an oblate-droplet impact, which is also used for the comparison to laser-ablation splashing in Section 4.1. This oblate droplet has a 15% difference between the major and minor diameters. Figures 5.1(f)-(j) show the splash produced by a more spherical droplet impact, where there is a difference between the major and minor diameters of 5%. In this splash, bubble formation is visible. Bisighini (2010) concludes that different impactor shapes explain the difference in splash evolution. Accordingly, a perfect spherical droplet causes the inward collapse resulting in bubble formation, while the deformed droplet-impact causes an upward crown formation followed by jetting [7], which is more similar to our laser-ablation results.

Following this interpretation, the pressure field created by the Gaussian laser profile could be expected to resemble the pressure profile generated by an oblate-droplet impact. The pressure profile resulting from laser impact can be estimated using Equation 2.7 introduced in theory Section 2.2. However, the pressure profile resulting from the oblate-droplet impact is unknown. Future droplet-impact simulations can shed light on this problem.

Our measured laser-ablation splash resembles the droplet-impact splash of an oblate droplet, as shown in Figure 4.1. It is likely that the shape of the pressure profile induced by laser impact does not fully match the pressure profile after impact of a spherical droplet. This qualitative comparison of experiments is an indication that the pressure profile resulting from oblate-droplet impact is more comparable to the laser-induced pressure profile. However, more droplet-impact

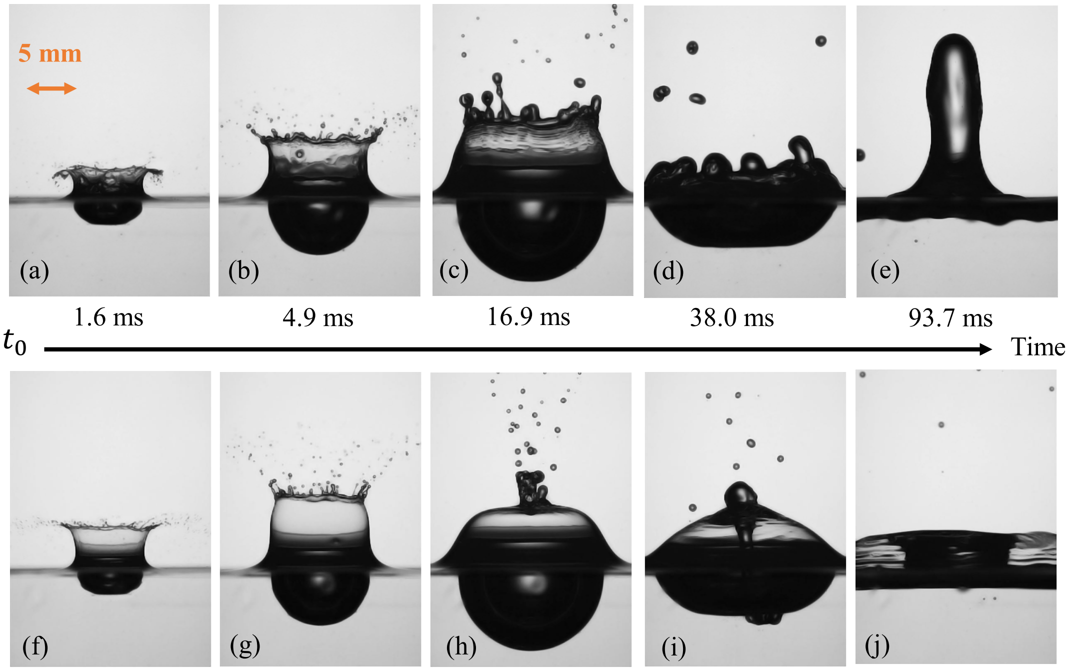

Figure 5.1: droplet-impact splashing over time, these two splashes are both the result of a 2.9 mm diameter droplet impacting acetic acid with 4.4 m/s. (a)-(e) Shows the splash evolution when an oblate droplet with a 15% deviation between minor and major diameter is used. (f)-(j) shows the splash evolution when this maximum deviation is 5%, figure courtesy of A. Bisighini [7].

literature visualizing deep-pool impact over time at high Weber number is desirable for precise qualitative comparison. For now, the comparison is restricted to one source. Preferably, in future work, the laser ablation experiments are compared to a body of droplet-impact research to compare similarities and disagreements.

5.2 Quantitative comparison analysis

In the quantitative comparison between laser-ablation splashing and droplet-impact splashing, the same splashes as shown in the visual comparison are compared (Section 4.1). The crown height and width evolution with time show similarities; at early-time, height and width increase with a decreasing expansion velocity, and at late-time, the width expansion velocity becomes approximately constant. However, the evolution of the crown height at late-time varies: the height of the droplet-impact crown decreases with an increasing downwards velocity, while the height of the laser-ablation crown decreases with an approximately constant velocity. To further compare both phenomena quantitatively, we use a dimensionless system defined by droplet-impact literature [4]. However, to transfer to that dimensionless system, a characteristic length scale and velocity have to be defined for the laser-ablation splash. As an Ansatz, the first measurable bottom width and crown velocity are used as defined in Section 3.3. In Section4.3 the potential of this Ansatz characteristic length scale and velocity are shown; the implementation of the Ansatz shows an empirical and theoretical match with the dimensionless width evolution of the droplet-impact splash. This definition of characteristic length scale and velocity is further discussed in the next section, but it is already used for this quantitative comparison.

Shifting to the dimensionless time domain with $\tau = t\frac{U}{D}$, and dimensionless height and width ($H^{*}=\frac{H}{D}$, $W^{*}=\frac{W}{D}$), can already explain the difference of two orders of magnitude in time, and one order of magnitude in size. Furthermore, in the early stages of the splash, when inertia dominates both gravity and surface tension, crown growth expands similarly. Two significant differences are observed between droplet-impact splashing and laser-ablation splashing in the dimensionless regime; the dimensionless magnitude of the crown height differs, and the shape of the height over time curve in the crown decline phase, as already mentioned, differs. The difference in shape is explained by the three orders magnitude difference in Bond number; Bo = 1 for this droplet-impact case, and Bo = 10^{-3} for this laser-ablation case. Moreover, the difference in magnitude of the dimensionless height is resolved in Figure 4.8; by using a laser energy of 30 mJ.

We have measured the height and top width of the laser-ablation crown, but in droplet-impact literature, also bottom width, crater dimensions, and crown angle are frequently measured [7, 8, 59, 60]. We were not able to measure these variables, as discussed in Section 3.2. Comparing more variables can give a more complete comparison of the splashing phenomena. Especially bottom width is of importance because the theory regarding crown width evolution introduced in Section 2.1.2 describes the bottom width. However, we apply this theory in Section 4.3.1 to the crown top width. We know that the top width is highly dependent on the inclination of the crown, for example, during bubble formation discussed in Section 5.1. Therefore, an exploratory analysis, which uses a first-order approach to measure crown bottom width with time is conducted, presented in appendix Section 8.4. The results show that the crown bottom width evolves similarly to the crown top width, which is to be expected when we look at Figure 4.1: there is a curvature in the crown edge, but the overall angle with the liquid film is close to 90°. The assumption of top and bottom width expansion being often similar, is also acknowledged in droplet-impact literature [6, 59, 61]. Therefore, we conclude that it is reasonable to analyze the crown width evolution by only using the top width over time, for measurements presented in this report.

In summary, we have shown that at early-time the crown evolution of a droplet-impact splash, and a laser-ablation splash, agree in terms of dimensionless crown height and dimensionless crown top width. This is achieved by defining a characteristic length scale and velocity to transfer to a dimensionless parameter space. Furthermore, the laser impact energy that matched well with the oblate-droplet impact at high Weber number is found.

5.3 Laser energy scan analysis

To answer the research question concerning the interchangeability of laser-ablation splashing and droplet-impact splashing, the decision on which relevant parameters have to be interchanged is essential. In the previous sections, we concluded that the crown evaluations of both phenomena can be very similar in dimensionless size, as well as shape if the appropriate characteristic parameters are chosen. The characteristic parameters for droplet-impact splashing are set by literature: the droplet size and droplet velocity. For laser-ablation splashing, we particularly study for varying laser energies, using constant laser spot size and constant pulse length. For this varying laser energy, the relevant length scale and velocity are chosen to be the first measurable width and first measurable crown velocity and are both laser energy-dependent. This width and velocity are compared to the droplet size and droplet velocity by using them in the inertial time $\tau = t\frac{U_L}{D_L}$ and dimensionless height and width $H^{*}=\frac{H}{D_L}$, $W^{*}=\frac{W}{D_L}$. This is an Ansatz, that is tested by using the parameters τ, H^{*}, and W^{*} for dimensionless comparison, and see if it scales as one would expect from droplet-impact literature. Furthermore, if this Ansatz proves successful, and the energy dependency of this characteristic length scale and velocity are determined, then we have found the scaling that connects laser energy from laser-ablation splashing and the droplet diameter and velocity from droplet-impact splashing.

In Figure 4.4, the energy dependency of the characteristic length scale is determined to follow $D_L = (208 \pm 6) + (4.1 \pm 0.4)E$ in the measured regime. In addition, the characteristic velocity is determined to follow U_L=$(8 \pm 1)E^{(0.4 \pm 0.1)}$. These relations are subsequently used in the following sections to analyze the dimensionless crown width and height over dimensionless time.

5.3.1 Width evolution analysis

After introducing the Ansatz inertial time and Ansatz length scale in the top width evolution, measurements are found to be approximately independent of laser energy, shown in Figure 4.5. Moreover, the initial starting width is subtracted because of the hypothesis that a droplet-impact crown starts at $W \approx 0$, while this is not expected for the laser-ablation crown. This difference is likely because the full width of the Gaussian laser spot impacts the liquid film at once, while the droplet starts entering the film only with the tip. After this subtraction, the theoretical crown width expansion fits over the initial crown expansion.

We define the initial crown expansion as the expansion phase up to $t = \tau_c/2$. The influence of the gravity is negligible over the whole crown evolution, and surface tension effects are assumed to be insignificant up to $t \approx \tau_c/2$. Results do not match up to $t = \tau_c$. This might be due to the used definition, which originates from research on spherical-droplet vibrations [46], it is probable that a spherical droplet and crown, are not fully comparable. For that reason, the exact value of the capillary time for a liquid crown could deviate. Still, the good agreement found between tho laser-ablation evolution and droplet-impact crown evolution up to $t = \tau_c/2$ is very encouraging.

The pre-factor, C_W, introduced in Equation 2.6 has a physical dependence on dimensionless film thickness for thin-film impact. However, even in thin-film impact, the theoretical values are rejected and replaced by empirical values [5, 6]. In addition, the scaling with film thickness does not hold for deep-pool impact, often defined as $h^* > 5$ [7]. Unfortunately, no empirical scaling is known. We assume that the laser-ablation experiments are in the deep-pool impact regime. Primarily because we observe jet formation after crown collapse (Figure 4.1j), in addition to the defined relevant length-scale (D_L) $<<$ film thickness (h). Therefore, we can not attribute a physical meaning to pre-factor C_W.

In conclusion, the dimensionless crown width evolution of the laser-ablation splash follows the same empirical and theoretical crown width evolution as the crown width of a droplet-impact splash at early-time. This result is realized after introducing the first measurable width as characteristic length scale, and first measurable velocity as characteristic velocity. However, more measurements over a larger laser energy domain should be performed in future experiments to check the validity of linear scaling of the characteristic length scale with laser energy and the power-law scaling of the characteristic velocity with laser energy.

5.3.2 Height evolution analysis

In Figure 4.6a, the dimensionless crown height of the laser-ablation splashing measurements are shown for various laser energies. The crown height in dimensionless parameter space is clearly more dependent on laser energy than crown width. Moreover, the collapse of crown height measurements for various laser energies up to $t \approx 3\tau_i$ presented in Figure 4.6b is not explicitly mentioned in literature describing droplet-impact splashing. However, experimental results and simulations by Roisman et al. (2002) and Liang et al. (2014) also show separating dimensionless crown height over time relations for different droplet velocities after $t > 4\tau_i$. Moreover, Roisman et al. (2002) explicitly state that the square root law with time introduced in Equation 2.6 for crown width evolution, can be applied for height [47]. Furthermore, in Section 4.3.2, we have shown that the crown height and width at constant laser energy evolve linearly with each other up to $t = \tau_c/2$. This relation corresponds to empirical results by Yarin and Weiss (1995), where the crown height over time of a droplet-impact splash is shown to scale linearly with crown width [5].

The empirical results of our laser-ablation splashing results, showing $W^* = C_W\sqrt{\tau}$ and $H = C_O(E) + C_E(E)W$, must imply that for the same data set $H^* = C_H(E)\sqrt{\tau}$ holds. This is presented in Figure 5.2. We observe an reasonable fit in the range $3\tau_i < t < \tau_c/2$. That the relation at very early-time ($t < 3\tau_i$) diverges from measurements, is expected, otherwise the relation presented in Section 4.3.2: $H^* = C_H\sqrt{\tau}$ at $t < 3\tau_i$, would be in direct contradiction with, $H^* = C_H(E)\sqrt{\tau}$, where the constant $C_H(E)$ is energy dependent. Comparison of the $C_H(E)$ for laser-ablation splashing, and $C_H(U, D)$ for droplet-impact splashing is left for future work.

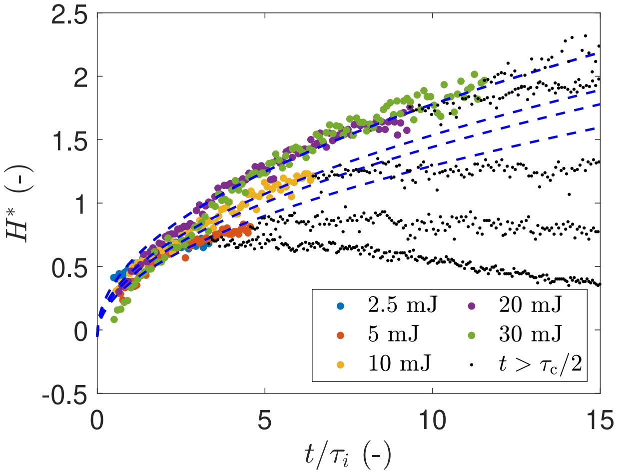

Figure 5.2: Evolution of the crown height in dimensionless parameter space for various laser energies using a constant spot size of 66 μm (FWHM) and a pulse length of 8 ns (FWHM). Only early-time data ($t < \tau_c/2$) is used for the fit shown in blue: $H^* = -0.05 + C_H(E)\sqrt{\tau}$. The fitting parameters $C_H(2.5) = 0.47 \pm 0.02$, $C_H(5) = 0.43 \pm 0.01$, $C_H(10) = 0.50 \pm 0.01$, $C_H(20) = 0.54 \pm 0.58$, and $C_H(30) = 0.57 \pm 0.01$ are found.

In conclusion, there is no theoretical underpinning proving the square root law with time for the crown height evolution in literature describing droplet-impact splashing. However, various authors do mention and empirically show this relation. Our results for the early-time crown height of the laser-ablation splash mostly agree with all that is presented in literature describing droplet-impact splashing. The found difference in crown height at late dimensionless time can be attributed to the relative importance of gravity at different length-scales, expressed in Bond numbers.

5.4 Height over width analysis

In Figure 4.7a, The mostly linear relation between crown height and width for different laser energies is presented. The linear relation is expected when both evolve similarly over time. This shows that even though the dimensionless height over time for different energies separate after $t = 3\tau_i$. This is due to different pre-factors, as shown in Figure 5.2.

The quadratic relation observed in Figure 4.7b is not previously described in literature. Unfortunately, not enough literature data is available to check this relation for droplet-impact splashing. However, given the established comparability of laser-ablation and droplet-impact splashing, it is probable that this effect also occurs in droplet-impact splashing. An attempt to a physical explanation for the observed $H \approx 0.01 + 0.33W^2$ is done here based on observations from droplet-impact literature and analysis:

Bisighini (2010) describes how crater expansion in deep-pool impact is hemispherical. Using this argument in the mass conservation law, comparing crater formation and crown growth, the following scaling relation holds in case of no mass-loss

$$WHe \propto W^3. \tag{5.1}$$

Where $W = 2R$, with R the radius of the crater, H crown height, and e the average crown thickness. No mass-loss can be assumed because during the initial crown growth, the volume of the detached droplets is negligible. Information concerning the average crown thickness can be obtained using the measured and known linear relation between height and width. This is made obvious by rewriting the mass conservation law as:

$$\frac{e}{W} \propto \frac{W}{H}. \tag{5.2}$$

Hereby we find that $e \propto W$ must hold to result in a linear relation between the width and height throughout the initial crown growth of a splash. From droplet-impact literature we know that film thickness primarily scales with viscosity and time as $e \propto \sqrt{\nu t}$ [10, 62]. This relation strengthens the argument that $e \propto W$, because also $W \propto \sqrt{t}$. Moreover, droplet-impact experiments conducted by Choge et al. (1999) to specifically study crown thickness over time were not able to do this accurately enough to conclude there was a correlation between film thickness and impact velocity [21]. Therefore, we can not check this hypothesis in droplet-impact literature. Furthermore, the increasing slope with increasing laser energies observed during our laser-ablation experiments indicates that the average thickness e, goes down with higher laser energies, following the proportionality relation in Equation 5.2.

In Figure 4.7a, we observe that the measurement with a laser energy of 2.5 mJ does not agree with the relation $H \approx 0.01 + 0.33W^2$. We hypothesize that this disparity is due to the hemispherical crater expansion, that is assumed for all energies. However, it is likely that the crater expansion is not hemispherical at sufficiently low laser energy. When the laser spot size is not negligible compared to the length scale over which fluid is displaced, crater expansion will not be hemispherical. We assume this is the case for the measurement with a laser energy of 2.5 mJ and spot size of 66 μm (FWHM).

5.5 Parameter space analysis

Laser-ablation splashing experiments were conducted with a fixed Gaussian, 66 μm FWHM spot size, with an 8 ns (FWHM) laser pulse length, within the laser energy range of 2.5 mJ - 30 mJ on a liquid tin film with a thickness of 3 mm. In this section, the limits of this parameter space are discussed by considering the influence of spot size, laser pulse length, spatial pulse shape, and film thickness.

An initial study of the laser focusing parameter is already performed, attached in appendix Section 8.3. Initial results show that the influence of spot size on crown growth is small compared to the influence of laser energy. However, the small number of measurements done on this subject make it inconclusive.

No measurements are performed on varying laser pulse lengths because of experimental limitations. However, the timescales of laser absorption ($\sim$ ns) and fluid displacements($\sim$ μs) are expected to be decoupled. Moreover, the plasma pressure impulse is dependent on laser intensity and pulse length as described in Equation 2.7, and the momenta transferred during the plasma expansion after laser impact on a liquid tin droplet scales as $U \propto \left(\frac{t_p}{10\text{ns}}\right)^{0.4}$, introduced in Equation 2.9. In these equations the pulse length is directly coupled to laser intensity and energy, at constant impulse or momentum transfer. Therefore, it is expected that crown evolution for various laser pulse lengths can be explained similarly as crown evolution for various laser energies.

Laser-ablation experiments performed in this report impact the liquid film in the focal point of the focusing lens; this creates a Gaussian intensity distribution in the focus spot. Spatial laser pulse shaping could be used to alter the splash. By changing the intensity distribution, the resulting plasma pressure profile is changed. However, to contribute to the interchangeability to droplet-impact splashing, more information concerning the pressure distribution during droplet impact is necessary. Nevertheless, spatial laser pulse shaping could contribute to the overall goal of suppressing the splash after laser impact. In Figure 5.1 the influence of a small change in impactor shape on crown formation is shown. Similar results can likely be achieved by changing the laser pulse shape.

The film thickness is kept approximately constant during experiments. According to literature on droplet-impact splashing, we know that the film thickness is an important parameter that has a significant influence on the resulting splash. Primarily at thin-film impact ($h* < 1$). However, when a thick film is used ($h^* > 5$) this effect disappears because the velocity profile induced by droplet impact has no interaction with the substrate [2, 4–8]. It would be beneficial to compare laser-ablation splashing experiments with various film thicknesses to droplet-impact splashing. Then, the assumption that the laser-ablation results presented were obtained in the deep-pool regime can be verified. Moreover, the results of laser-ablation measurements at various film thicknesses can contribute to the definition of a more accurate characteristic length scale. In addition, measurements with thin films present the opportunity to research the influence of substrate geometry.

In summary, expanding the parameter space is beneficial to both answering the research question, and to contribute to suppression of laser-ablation splashes. With an increased parameter space, assumption made can be confirmed or corrected, and the overarching goal of suppression of laser-ablation splashing can be researched by, for example, spatial laser pulse shaping, and changing substrate geometry.

Chapter 6

Summary and outlook

In this thesis, we investigated if droplet-impact splashing and laser-ablation splashing are commutable. We found qualitatively and quantitatively a similar fluid dynamical response of a liquid tin film after laser impact, compared to droplet impact on acetic acid, at early dimensionless time. These similarities were found even with an order of magnitude difference in length scale between both phenomena. The found difference in crown height at late dimensionless time can be attributed to the relative importance of gravity at different length scales, expressed in Bond numbers.

To find out if droplet-impact splashing and laser-ablation splashing are fully commutable, a predictive model must hold. In such a model, the independent variables for laser-ablation: laser energy, laser spot size, and pulse length, should be connected to the independent variables for droplet impact: droplet size, and droplet velocity. These variables have to be linked such that we should be unable to see from the splash dynamics, whether we are dealing with droplet impact, or laser impact. Furthermore, if a set of independent variables of a specific droplet-impact splash are known, laser impact should be able to recreate that splash, by merely converting the droplet-impact variables to laser-impact variables.

We are not quite there yet, we performed laser-ablation experiments with different laser energies, but constant spot size and pulse length, the results are compared to the limited applicable droplet-impact literature available. The dimensionless crown growth over time, especially width over time, matches well both empirical and theoretical droplet-impact relations. The relevant length scale and velocity associated with these dimensionless results are found to be laser energy-dependent. The laser energy dependency in the measured laser energy regime (2.5 mJ - 30 mJ) is presented in Table 6.1.

Table 6.1: Characteristic length scale and velocity of the droplet-impact splash and the laser-ablation splash, that lead to a similar dimensionless parameter space. The laser energy dependent length scale and velocity are found at a constant Gaussian 66 μm FWHM spot size, with an 8 ns (FWHM) laser pulse length, within the measured range 2.5 mJ - 30 mJ.

	Droplet-impact splash	Laser-ablation splash
Characteristic length scale (D)	Droplet diameter (D_D)	$D_L\,(\mu\text{m}) = 208 + 4E\,(\text{mJ})$
Characteristic velocity (U)	Droplet velocity (U_D)	$U_L\,(\text{m/s}) = 8E^{0.4}(\text{mJ})$

Using the relations found in Table 6.1, droplet impact can be interchanged with laser impact with a certain laser energy, at-least for the initial growth phase $t < \tau_c/2$, in dimensionless parameter space. In addition, it is expected that conducting both experiments in the similar length scale regime, the discrepancy by influence of gravity disappears and both phenomena will overlay even more.

To accurately investigate the commutability of laser-ablation and droplet-impact splashing, more research into droplet-impact splashing has to be done, in addition to the expansion of laser-ablation research discussed in Section 5.5. This could be done by reproducing a scaling study in the droplet-impact domain, preferably using liquid tin and a similar characteristic length scale as in laser-ablation experiments, to obtain a similar Bond number. Moreover, if one focuses on the crown evolution, also simulations on crown behavior could be done. Simulations of crown and crater behavior after droplet impact have been done in the past [63]. Removing the volume of the droplet and only applying an initial pressure field is a first-order approximation of laser impact. Moreover, laser-ablation to pressure field conversions can already be used from literature [38, 52]. Furthermore, a more detailed laser-ablation pressure profile could be obtained using the radiation-hydrodynamic software package RALEF-2D [64], as done by Kurilovich et al. (2018) for laser impact on droplets [39].

To apply the research presented in this thesis in the broader framework of EUV light production, and divertor technology in nuclear fusion, more work needs to be done. This study was not designed to simulate the heat fluxes caused by plasma instabilities in nuclear fusion reactors, such as disruptions or edge localized modes. Heat fluxes caused by plasma instabilities take $\sim$ms, which is a 6 orders of magnitude difference with the $\sim$ns laser pulses. Furthermore, there is a 9 order of magnitude difference in deposition area and 2 orders of magnitude in peak power [22]. Moreover, the heat fluxes in a nuclear fusion device will not be circular like the focused laser spot. Therefore, the scaling of our results towards nuclear fusion engineering is difficult. Nevertheless, in-depth knowledge on how to suppress splashing, which can be obtained in future work, for example, by optimizing substrate geometry, could be incorporated in liquid metal divertor design.

The current EUV source is a complex, multi-faceted system. Contamination control is one of the many facets. Already, droplet fragments, but also atomic and ionic debris, are being minimized [31]. Changing from the currently used mass-limited target to a liquid film, researched in this thesis, is most probably not feasible for high power laser impact, because of contamination limits set by the multilayer mirrors used in the EUV source [65, 66]. However, an alternative could be to use a rarefaction pulse on the liquid film. The rarefaction pulse is strong enough to create a tin plasma, however, not strong enough for a substantial fluid dynamical response in the form of a splash. This plasma is subsequently shot with the main laser pulse, parallel to the liquid film, the energy of the main laser is coupled into the plasma via inverse bremsstrahlung and the plasma conditions required to emit in-band EUV radiation (13.5 nm ± 2%)[31] are reached. In case the liquid film is used in combination with a rarefaction pulse, research into suppressing the splash is still of value for two reasons. First, the maximum energy of the rarefaction pulse is likely to be limited by the fluid dynamical response of the liquid film. Second, the main laser will add energy to the plasma close to the surface of the liquid film, created by the rarefaction pulse. This plasma will subsequently expand further and apply pressure to the liquid film, which can cause splashing.

Chapter 7

Conclusion

In this thesis, the first step towards commutability of laser-ablation and droplet-impact splashing is presented. The crown evolution of laser ablation on a liquid tin film is studied experimentally and compared to crown evolution after droplet impact. This comparison is made both qualitatively, as well as quantitatively. Good agreement is found between the laser-ablation crown and droplet-impact crown in dimensionless parameter space, where it is expected. Small differences can be attributed to the influence of gravity in droplet-impact studies, while the influence of gravity is negligible on the small length scales of the laser-ablation regime.

A laser energy scaling study is performed to study the laser-ablation splash. The dimensionless crown width evolution is found to be independent of laser energy, up to the capillary time scale, by introducing the characteristic length scale and velocity. The collapse of all measurements in the dimensionless domain is expected from droplet-impact literature. Furthermore, the square root relation over time in dimensionless units found, agrees with the theoretical prediction of a drop impacting a thin film. The measurements for dimensionless height over time only partly collapse. Moreover, measurements with varying laser energy follow the square root law, but with varying pre-factors.

A linear relation between the height and width is measured during the crown growth phase after laser-ablation; this is also expected from droplet-impact literature. In addition, the slope of the linear relations is studied for multiple laser energies and found to follow $H = C_0(E) + C_E(E)W$ with $C_0(E)$ and $C_H(E)$ energy-dependent constants. These energy dependent constants evolve approximately such that for the collection of all measured energies $H \approx 0.01 + 0.33W^2$ is obtained.

In summary, we have shown that there is a strong indication to believe that droplet-impact splashing and laser-ablation splashing are interchangeable. However, more steps have to be taken to prove full interchangeability of laser ablation and droplet impact in the splashing regime, such as spot size variation and laser pulse shaping, as well as measuring over a larger laser energy domain. Furthermore, a study on crown formation in deep-pool droplet-impact is necessary to solve the problem of limited research done on this topic in literature. Nevertheless, the powerful analogy between laser impact and droplet impact can be used to shed light on the unknown field of laser-ablation splashing of liquids. This knowledge can then be applied to suppress liquid metal splashing in both liquid metal divertor technology and in the design of a new EUV source for nanolithography.

Acknowledgements

I want to thank all people involved in this project. In particular, I thank my formal supervisors: Oscar Versolato, Peter Rindt, Niek Lopes Cardozo, and Job Beckers, for their constructive feedback over the whole duration of the project. Also, I would like to thank my informal supervisor, Bo Lui, for the useful discussions and help to get the experimental set-up up and running.

The whole EUV plasma processes group at ARCNL made me feel welcome during my stay. I would especially like to thank the technician Laurens van Buuren, for the exceptional help I got when, for example: components of both imperial and metric sizes had to be combined, gas leaks had to be fixed, or the target-holder needed a make over to adjust for the complete modification of the optical-laser path.

Furthermore, a big thanks go to the mechanical engineering department of AMOLF, especially to Henk-Jan Boluit, who helped design the target and target-holder. Moreover, I am grateful for Philips Dunlee producing the tungsten target using additive manufacturing. Additionally, I thank the Prototype and Equipment Center at the TU/e for the finishing of the tungsten targets. Likewise, I thank Ronald Wolbeer from the DIFFER workshop, who made his vacuum oven available for our experimental wetting attempts.

From early on in the project, I was able to get in touch with researchers that helped me identify the challenges of my project using their experience. From VDL ETG this were John Vogels and Paul Blom. At ASML, Sander Baltussen gave the insight that wetting would be a significant challenge; later on, Michel Riepen helped with many more attempts to create a thin liquid film of tin on top of the tungsten substrate. At TU/e, Hanneke Gelderblom introduced me in the, for me unknown, field of fluid dynamics, more specifically, the physics of splashing.

Last but not least, I would like to recognize the importance of my lab partner, Job Duffhues, who helped with everything, from target design to beam alignment to operating the set-up.

Bibliography

[1] M. R. Panão and A. L. N. Moreira, “Flow characteristics of spray impingement in pfi injection systems”, Experiments in Fluids **39**, 364–374 (2005).

[2] G. Liang and I. Mudawar, “Review of mass and momentum interactions during drop impact on a liquid film”, International Journal of Heat and Mass Transfer **101**, 577–599 (2016).

[3] A. Worthington, *A study of splashing* (London: Longmans, Green. 129 pp, 1908).

[4] A. L. Yarin, “Drop impact dynamics: splashing, spreading, receding, bouncing…”, Annu. Rev. Fluid Mech. **38**, 159–192 (2006).

[5] A. Yarin and D. Weiss, “Impact of drops on solid surfaces: self-similar capillary waves, and splashing as a new type of kinematic discontinuity”, Journal of fluid mechanics **283**, 141–173 (1995).

[6] G. Cossali, G. Brunello, A. Coghe, and M. Marengo, “Impact of a single drop on a liquid film: experimental analysis and comparison with empirical models”, in Italian congress of thermofluid dynamics uit, ferrara, Vol. 30 (1999).

[7] A. Bisighini, “Single and double drop impacts onto deep and thick liquid layers”, PhD thesis (2010).

[8] A. Geppert, A. Terzis, G. Lamanna, M. Marengo, and B. Weigand, “A benchmark study for the crown-type splashing dynamics of one-and two-component droplet wall–film interactions”, Experiments in Fluids **58**, 172 (2017).

[9] E. Castillo-Orozco, A. Davanlou, P. K. Choudhury, and R. Kumar, “Droplet impact on deep liquid pools: rayleigh jet to formation of secondary droplets”, Physical Review E **92**, 053022 (2015).

[10] R. L. Vander Wal, G. M. Berger, and S. D. Mozes, “Droplets splashing upon films of the same fluid of various depths”, Experiments in fluids **40**, 33–52 (2006).

[11] A. Geppert, D. Chatzianagnostou, C. Meister, H. Gomaa, G. Lamanna, and B. Weigand, “Classification of impact morphology and splashing/deposition limit for n-hexadecane”, Atomization and Sprays **26** (2016).

[12] E. Villermaux, “Fragmentation”, Annu. Rev. Fluid Mech. **39**, 419–446 (2007).

[13] S. Thoroddsen, “The ejecta sheet generated by the impact of a drop”, Journal of Fluid Mechanics **451**, 373–381 (2002).

[14] G. Cossali, A. Coghe, and M. Marengo, “The impact of a single drop on a wetted solid surface”, Experiments in fluids **22**, 463–472 (1997).

[15] B. Ray, G. Biswas, and A. Sharma, “Regimes during liquid drop impact on a liquid pool”, Journal of Fluid Mechanics **768**, 492–523 (2015).

[16] A. Alam, H. Kai, and K. Suzuki, "Two-dimensional numerical simulation of water splash phenomena with and without surface tension", Journal of marine science and technology **12**, 59–71 (2007).

[17] K.-L. Pan, K.-R. Cheng, P.-C. Chou, and C.-H. Wang, "Collision dynamics of high-speed droplets upon layers of variable thickness", Experiments in fluids **45**, 435–446 (2008).

[18] C. Josserand, P. Ray, and S. Zaleski, "Droplet impact on a thin liquid film: anatomy of the splash", Journal of Fluid Mechanics **802**, 775–805 (2016).

[19] A. Bisighini, G. E. Cossali, C. Tropea, and I. V. Roisman, "Crater evolution after the impact of a drop onto a semi-infinite liquid target", Physical Review E **82**, 036319 (2010).

[20] G. Liang, Y. Guo, S. Shen, and Y. Yang, "Crown behavior and bubble entrainment during a drop impact on a liquid film", Theoretical and Computational Fluid Dynamics **28**, 159–170 (2014).

[21] A. Coghe, G. Brunello, G. Cossali, M. Marengo, and M.-I. TeMPE-CNR, "Single drop splash on thin film: measurements of crown characteristics", in Ilass europe, Vol. 99, 6 (1999).

[22] S. Pestchanyi, R. Pitts, and M. Lehnen, "Simulation of divertor targets shielding during transients in iter", Fusion Engineering and Design **109**, 141–145 (2016).

[23] P. Rindt, "The potential of liquid-metal 3d-printed heat shields for fusion reactors", PhD thesis (Technische Universiteit Eindhoven, 2019), pp. 103–156.

[24] G. Nallo, G. Mazzitelli, L. Savoldi, F. Subba, and R. Zanino, "Self-consistent modelling of a liquid metal box-type divertor with application to the divertor tokamak test facility: li versus sn", Nuclear Fusion **59**, 066020 (2019).

[25] T. Morgan, P. Rindt, G. Van Eden, V. Kvon, M. Jaworksi, and N. L. Cardozo, "Liquid metals as a divertor plasma-facing material explored using the pilot-psi and magnum-psi linear devices", Plasma Physics and Controlled Fusion **60**, 014025 (2017).

[26] P. Rindt, T. Morgan, M. Jaworski, and N. L. Cardozo, "Power handling limit of liquid lithium divertor targets", Nuclear Fusion **58**, 104002 (2018).

[27] G. Van Eden, T. Morgan, D. Aussems, M. Van Den Berg, K. Bystrov, and M. Van De Sanden, "Self-regulated plasma heat flux mitigation due to liquid sn vapor shielding", Physical review letters **116**, 135002 (2016).

[28] Y. Shi, G. Miloshevsky, and A. Hassanein, "Boiling induced macroscopic erosion of plasma facing components in fusion devices", Fusion Engineering and Design **86**, 155–162 (2011).

[29] G. Miloshevsky and A. Hassanein, "Modelling of kelvin–helmholtz instability and splashing of melt layers from plasma-facing components in tokamaks under plasma impact", Nuclear fusion **50**, 115005 (2010).

[30] D. Salzmann, *Atomic physics in hot plasmas*, Vol. 97 (Oxford University Press on Demand, 1998).

[31] O. O. Versolato, "Physics of laser-driven tin plasma sources of euv radiation for nanolithography", Plasma Sources Science and Technology **28**, 083001 (2019).

[32] M. Purvis, I. V. Fomenkov, A. A. Schafgans, M. Vargas, S. Rich, Y. Tao, S. I. Rokitski, M. Mulder, E. Buurman, M. Kats, et al., "Industrialization of a robust euv source for high-volume manufacturing and power scaling beyond 250w", in Extreme ultraviolet (euv) lithography ix, Vol. 10583 (International Society for Optics and Photonics, 2018), p. 1058327.

[33] I. Fomenkov, D. Brandt, A. Ershov, A. Schafgans, Y. Tao, G. Vaschenko, S. Rokitski, M. Kats, M. Vargas, M. Purvis, et al., "Light sources for high-volume manufacturing euv lithography: technology, performance, and power scaling", Advanced Optical Technologies **6**, 173–186 (2017).

[34] V. Craciun, N. Bassim, R. Singh, D. Craciun, J. Hermann, and C. Boulmer-Leborgne, “Laser-induced explosive boiling during nanosecond laser ablation of silicon”, Applied surface science **186**, 288–292 (2002).

[35] A. Semerok, C. Chaléard, V. Detalle, J.-L. Lacour, P. Mauchien, P. Meynadier, C. Nouvellon, B. Sallé, P. Palianov, M. Perdrix, et al., “Experimental investigations of laser ablation efficiency of pure metals with femto, pico and nanosecond pulses”, Applied Surface Science **138**, 311–314 (1999).

[36] J. H. Yoo, S. Jeong, R. Greif, and R. Russo, “Explosive change in crater properties during high power nanosecond laser ablation of silicon”, Journal of Applied physics **88**, 1638–1649 (2000).

[37] H. Gelderblom, H. Lhuissier, A. L. Klein, W. Bouwhuis, D. Lohse, E. Villermaux, and J. H. Snoeijer, “Drop deformation by laser-pulse impact”, Journal of fluid mechanics **794**, 676–699 (2016).

[38] D. Kurilovich, A. L. Klein, F. Torretti, A. Lassise, R. Hoekstra, W. Ubachs, H. Gelderblom, and O. O. Versolato, “Plasma propulsion of a metallic microdroplet and its deformation upon laser impact”, Physical review applied **6**, 014018 (2016).

[39] D. Kurilovich, M. M. Basko, D. A. Kim, F. Torretti, R. Schupp, J. C. Visschers, J. Scheers, R. Hoekstra, W. Ubachs, and O. O. Versolato, “Power-law scaling of plasma pressure on laser-ablated tin microdroplets”, Physics of Plasmas **25**, 012709 (2018).

[40] J. Freeman, S. Harilal, B. Verhoff, A. Hassanein, and B. Rice, “Laser wavelength dependence on angular emission dynamics of nd: yag laser-produced sn plasmas”, Plasma Sources Science and Technology **21**, 055003 (2012).

[41] J. Hernandez-Rueda and D. van Oosten, “Dynamics of ultrafast laser ablation of water”, arXiv preprint arXiv:1810.06946 (2018).

[42] *The american heritage dictionary of the english language*, American Heritage Dictionary of the English Language (Houghton Mifflin Harcourt, 2011).

[43] A. Prosperetti and H. N. Oguz, “The impact of drops on liquid surfaces and the underwater noise of rain”, Annual Review of Fluid Mechanics **25**, 577–602 (1993).

[44] R. Krechetnikov and G. M. Homsy, “Crown-forming instability phenomena in the drop splash problem”, Journal of colloid and interface science **331**, 555–559 (2009).

[45] J. M. Fullana and S. Zaleski, “Stability of a growing end rim in a liquid sheet of uniform thickness”, Physics of Fluids **11**, 952–954 (1999).

[46] J. Bostwick and P. Steen, “Capillary oscillations of a constrained liquid drop”, Physics of Fluids **21**, 032108 (2009).

[47] I. Roisman and C. Tropea, “Impact of a drop onto a wetted wall: description of crown formation and propagation”, Journal of Fluid Mechanics **472**, 373–397 (2002).

[48] H. Shetabivash, F. Ommi, and G. Heidarinejad, “Numerical analysis of droplet impact onto liquid film”, Physics of Fluids **26**, 012102 (2014).

[49] D. Hudgins, N. Gambino, B. Rollinger, and R. Abhari, “Neutral cluster debris dynamics in droplet-based laser-produced plasma sources”, Journal of Physics D: Applied Physics **49**, 185205 (2016).

[50] T. Ando, S. Fujioka, H. Nishimura, N. Ueda, Y. Yasuda, K. Nagai, T. Norimatsu, M. Murakami, K. Nishihara, N. Miyanaga, et al., “Optimum laser pulse duration for efficient extreme ultraviolet light generation from laser-produced tin plasmas”, Applied physics letters **89**, 151501 (2006).

[51] P. Mora, “Theoretical model of absorption of laser light by a plasma”, The Physics of Fluids **25**, 1051–1056 (1982).

[52] R. Fabbro, P. Peyre, L. Berthe, and X. Scherpereel, “Physics and applications of laser-shock processing”, Journal of laser applications **10**, 265–279 (1998).

[53] C. Phipps Jr, T. Turner, R. Harrison, G. York, W. Osborne, G. Anderson, X. Corlis, L. Haynes, H. Steele, K. Spicochi, et al., “Impulse coupling to targets in vacuum by krf, hf, and co2 single-pulse lasers”, Journal of Applied Physics **64**, 1083–1096 (1988).

[54] Z. Ye, X. Ma, P. He, Z. Wang, Q. Liu, Q. Yan, J. Wei, K. Zhang, and F. Gou, “The investigation of plasma-induced wettability of liquid tin-capillary porous system”, Nuclear Materials and Energy **20**, 100694 (2019).

[55] A. E. Siegman, “Defining, measuring, and optimizing laser beam quality”, in Laser resonators and coherent optics: modeling, technology, and applications, Vol. 1868 (International Society for Optics and Photonics, 1993), pp. 2–12.

[56] I. R. Peters, D. van der Meer, and J. M. Gordillo, “Splash wave and crown breakup after disc impact on a liquid surface”, Journal of fluid mechanics **724**, 553–580 (2013).

[57] J. Duffhues, “Laser produced plasma crown formation and secondary droplet atomization on a liquid tin layer”, MA thesis (University of Technology Eindhoven, the Netherlands, 2020).

[58] M. Xu, C. Li, C. Wu, X. Chen, and S. Lu, “Regimes during single water droplet impacting on hot ethanol surface”, International Journal of Heat and Mass Transfer **116**, 817–824 (2018).

[59] G. Cossali, M. Marengo, A. Coghe, and S. Zhdanov, “The role of time in single drop splash on thin film”, Experiments in Fluids **36**, 888–900 (2004).

[60] I. V. Roisman, N. P. van Hinsberg, and C. Tropea, “Propagation of a kinematic instability in a liquid layer: capillary and gravity effects”, Physical Review E **77**, 046305 (2008).

[61] G. Liang, Y. Guo, and S. Shen, “Gas properties on crown behavior and drop coalescence”, Numerical Heat Transfer, Part B: Fundamentals **65**, 537–553 (2014).

[62] M. V. Gielen, P. Sleutel, J. Benschop, M. Riepen, V. Voronina, C. W. Visser, D. Lohse, J. H. Snoeijer, M. Versluis, and H. Gelderblom, “Oblique drop impact onto a deep liquid pool”, Physical review fluids **2**, 083602 (2017).

[63] S. A. Reijers, B. Liu, D. Lohse, and H. Gelderblom, “Oblique droplet impact onto a deep liquid pool”, arXiv preprint arXiv:1903.08978 (2019).

[64] M. Basko, J. Maruhn, and A. Tauschwitz, “Development of a 2d radiation-hydrodynamics code ralef for laser plasma simulations”, GSI report **1**, 410 (2010).

[65] V. Bakshi, *Euv lithography* (2nd Edition ed. (SPIE Press, 2018)).

[66] V. Bakshi, *Euv lithography*, Vol. 178 (Spie Press, 2009).

[67] W. Forsythe and E. Adams, “Radiating characteristics of tungsten and tungsten lamps”, JOSA **35**, 108–113 (1945).

[68] J. Oliver and S. Mason, “Liquid spreading on rough metal surfaces”, Journal of materials science **15**, 431–437 (1980).

Chapter 8

Appendix

Section 1 and 2 of this Chapter give more insight in to the development of the experimental set-up, which initially was build with a different goal in mind. This different goal had a large influence on target design. In Section 3 prelimairy experiments using varying laser spot sizes are presented, however, more work has to be done before conclusions can be drawn. In Section 4 the difficulties with bottom crown detection are discussed. In Section 5 the Matlab script used to extract variables from grey-scale images is given. Section 6 describes methods used to obtain uncertainty intervals.

8.1 Film thickness control

The initial goal of the project was to change layer thickness and do measurements at thin layers (~ 0.1 mm). Furthermore, laboratory safety personal at ARCNL expressed desire to keep the laser parallel to the optical table, which means the liquid target had to be put on vertically as also shown in figure 8.1. If the liquid target system is small enough (Bo<<1) and the binding energy between the liquid and substrate is negative, capillary forces are responsible for a stable liquid metal film, even in vertical orientation. The built system to vary layer thickness is schematically illustrated in figure 8.1. The system uses a pressure difference ($\Delta P = P_{II} - P_I$) between the operating chamber and tin supply line. The resulting force from ΔP pushes tin in or out of the target substrate. This system is able to control film thickness when the substrate has an closed liquid surface. However, sufficient wetting for thin films was not achieved. This is further discussed in Section 2.1 of this chapter. Important consideration is that in this phase of the project the target was orientated vertically, this was later changed to a horizontal orientation, because thicker tin layers flow downwards by gravity.

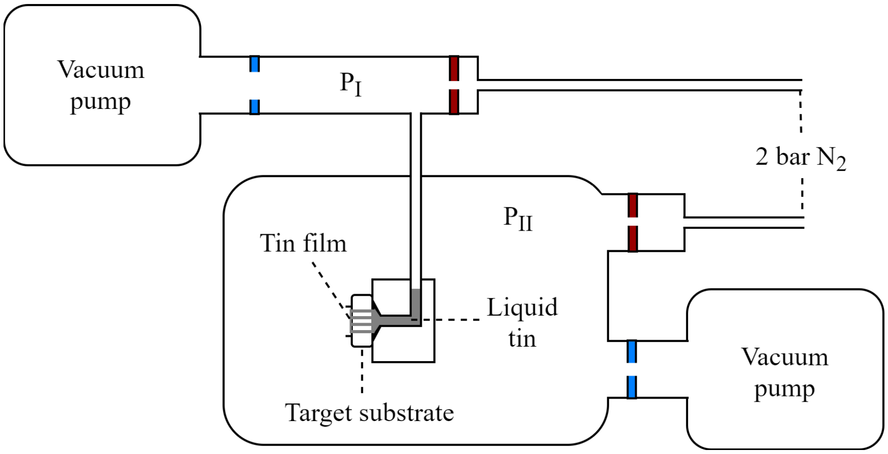

Figure 8.1: Pressure control system designed to achieve a pressure difference $\Delta P = P_{II} - P_I$ such that the tin film thickness can be changed. In blue adjustable valves to the vacuum pumps are depicted, and in red adjustable valves to the high pressure nitrogen line are shown. By balancing the size of the apertures stable controllable pressures P_I and P_{II} can be achieved.

8.2 Target substrate

With the goal of doing measurements over different thin liquid layer thicknesses in mind the targets were designed. The design requirements for the target were

1. **Temporarily durable against laser pulses of $\sim 10^8$ J/m^2.**

The target has to be durable in case the liquid thin film gets penetrated or is dewetted by the repetitive laser pulses. In the closed vacuum chamber it is possible that we do not observe this incorrect measurement immediately, but only after ∼100 laser pulses. It is important that the target is still usable after this.

2. **Multiple laser impact locations, in case of failure (≥ 4).**

In case the previously mentioned laser impact without protective liquid layer does result in local damage, it is desirable that the target is designed such that if a local measurement location has become unusable, other measurement locations are still present. These locations function as a back-up.

3. **Contact surface with liquid as smooth as possible (Roughness$\sim$ 1 Ra).**

For these experiments effects because of geometries underneath the liquid film are not wanted. Accordingly, the roughness of the target substrate has to be controlled [4]. There is no clear roughness threshold, therefore we aim for best possible roughness within our production capability using electrical discharge machining.

4. **Liquid tin supply via bottom side of target.**

To operate a film thickness control system, a pressure difference needs to be present between two separated areas with a tin reservoir in the middle. With limited space in the operating chamber because optical access lines are needed, this reservoir is made in the target holder. Therefore, tin has to be supplied from the bottom side of the target.

5. **Distribution of tin over measurement locations.**

The liquid tin has to be spread over the measurement locations equally, such that the film thickness can be determined from a side-view.

6. **The target material is nonreactive and has a low solubility in liquid tin.**

The liquid tin has to preserve its fluid properties and influence of contamination have to be negligible.

7. **Free line of sight parallel and perpindicular to surface.**

Perpendicular to the surface a high power laser is incoming. In addition, parallel to the surface at least one line of sight has to be free to operate the shadowgraphy system including back-light and camera.

8. **Length-scale calibration in field of view.**

If images are captured by the shadowgraphy system, a length-scale calibration is necessary to determine pixel-size. This can be done by inserting a pillar with known height in the field of view. The size of this pillar is determined by fabrication quality such that the uncertainty is less than 5%.

9. **Compatible with target-holder that already exists.**

There already is a target-holder that consists of a copper block and heater elevated by a bar screwed on the bottom of the operating chamber, depicted in figure 3.2. On this target-holder a cylinder can be clammed, the clamming system determines the outer dimensions of the target substrate.

The main advantages of using tungsten are among other things its high melting temperature, its reasonable thermal conductivity and the fact that it does not react and has a low solubility with liquid tin. Furthermore, from the point of view of the fusion application, it is interesting to realize that tungsten is often used in a liquid metal divertor. Tin is used because of the lithography applications, as well as the possible application in a liquid metal divertor. For this project there was access to additive tungsten manufacturing at Philips. The result is seen in figure 3.4. Channels through the center of the target supply tin to the surface of the target seen in figure 3.4c. To promote wetting, four locations are surrounded by a canal that can be filled with liquid tin, forming islands. Tin can be pumped up through the channels using the pumping system in figure 8.1. The liquid tin was intended to cover the islands with a stable film of liquid tin. Furthermore, pillars with a known height are added on the side to calibrate the length scale in shadowgraphy images. To prevent the pillars to be covered with tin themselves, channels were made between the tables and the pillar to separate the pillar from the tin.

8.2.1 Wetting

To achieve wetting, the liquid and substrate have to interact such that it is energetically beneficial to wet. Hence, tungsten and liquid should not repel each other. A similar laser ablation demo experiment using a tungsten liquid metal divertor model designed by Peter Rindt [23] using tin as liquid metal was done in 2018 at ARCNL. Herein, also the vertical orientation was used, and a seemingly stable tin film was formed. For that reason this vertical tin film approach was expected to work.

The same procedure was followed. Solid 99.99% tin was put on the tungsten target in the vacuum oven that used an inductive current to heat the tungsten. No temperature measurement was present, however, the tungsten had a yellow glow, hence temperature was above 1000 K [67]. The tin visually spreads over the tungsten target. However, when put vertical in the set-up, tin would move down and form a droplet on the bottom of the target. The following procedures were tried to create a stable tin film on the substrate.

- Apply tin in vacuum oven on substrate (T>1000 K, P=10^{-6} mbar).
- Apply tin in hydrogen radical oven on substrate.
- Use hydrogen background during experiment (0.05 mbar).
- Try multiple tungsten substrate roughness (roughness of 1 Ra to 20 Ra).

The first three processes try to minimise the contamination and oxidation of the tin as well as the tungsten. Contamination and oxidation have been demonstrated to have a negative effect on the wetting by Ye et al [54]. Additionally, the last process is done because the roughness of a substrate can have influence on the wetting behaviour, this is empirically shown by Oliver et al. [68]. Sufficient wetting to perform laser ablation experiments on a thin liquid tin film was not achieved during this project. Therefore, we diverted towards a thick layer of tin ($\sim$ mm) on a horizontal target, which was loaded in the vacuum oven. A ceramic cylinder kept the volume of tin in the middle of the substrate as shown in figure 3.4d. Furthermore, a tin repellent marker is used around pillars and in the moat to prevent wetting there. The tin repellent marker is borrowed from the DIFFER workshop and not properly branded. However, similar products exists of which the list of ingredients ordered weight based is: trade secret transition metal oxide, isopropyl acetate, isopropanol, petroleum distillates, methyl N. A. Ketone, Methyl n-P Ketone, Ethyl 3-Ethoxypropionate. The following section describes how the rest of the experiment is constructed to laser ablate this liquid tin bath and image the resulting splash.

8.3 Initial studies of focusing parameter

By varying the size of the focused laser spot the total energy deposited on the film stays constant. However, the fluence (J/m^2) scales inversely with the area of the spot. Doing experiments with different spot sizes one can investigate if energy, fluence, or both are the driving variables for crown evolution. In figure 8.2 the height and width evolution is plotted for three different energies. Within these energies measurements with different laser spot diameters are done. Remarkably, one can conclude that the width of crown is hardly dependent on the width of the laser spot. In addition, one sees that the height evolution is mainly dependent on energy but also slightly on spot size. Notable is that at low energy (5 mJ) a larger spot size (116 um seen in red) results a slightly higher crown, while at high energy (20 mJ) a larger spot size (135 um seen in purple) results in a smaller crown. At 10 mJ all spot sizes overlay.

In addition initial crown width and crown velocity are also extracted for these measurements plotted in figure 8.3. An interesting observation is that a larger spot size initially results in a larger crown width in the first microseconds, however, this does not hold during further evolution as seen in figure 8.2b. More measurements have to be done to create more frames to analyse, such that the initial velocity over laser energy can be accurately determined in figure 8.3b.

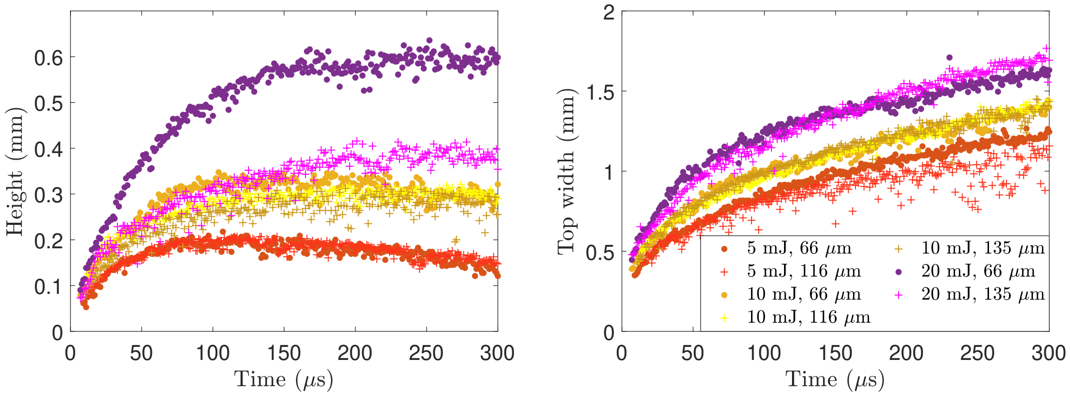

(a) **(b)**

Figure 8.2: Crown evolution over time after laser impact on liquid tin, using different laser energies. Short laser pulses of 8 ns are focused to Gausian spot sizes with FWHM of 66, 116, and 135 μm. Crown height (a) and crown width (b) over time for laser energies between 5 mJ and 20 mJ are plotted.

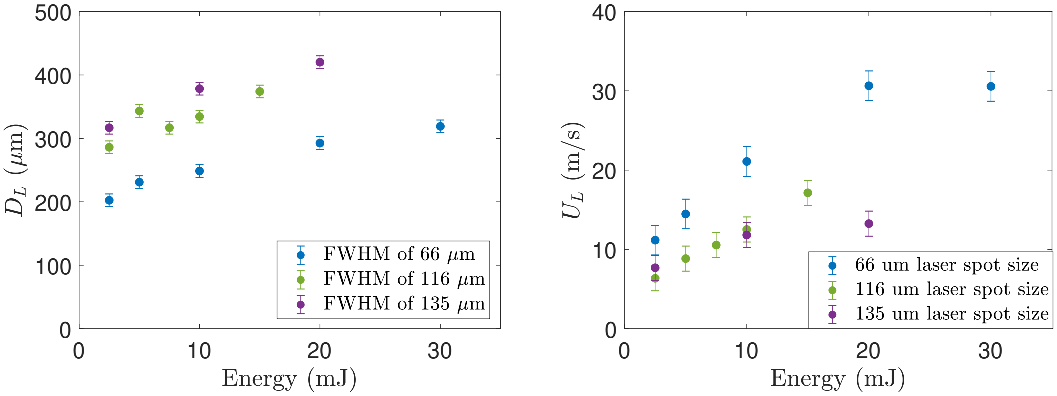

(a) **(b)**

Figure 8.3: The first observable crown width (a) and crown velocity (b) are shown for different laser energies using three different spot sizes and a pulse length of 8 ns. In figure 4.4b.

8.4 Exploratory analysis bottom width evolution

In figure 8.4 both measured bottom and top width are shown for the laser energy scan. The measurements with laser energies between 2.5 mJ and 20 mJ mostly agree. The bottom width for the laser energy of 30 mJ is not plotted, because this was not properly detected.

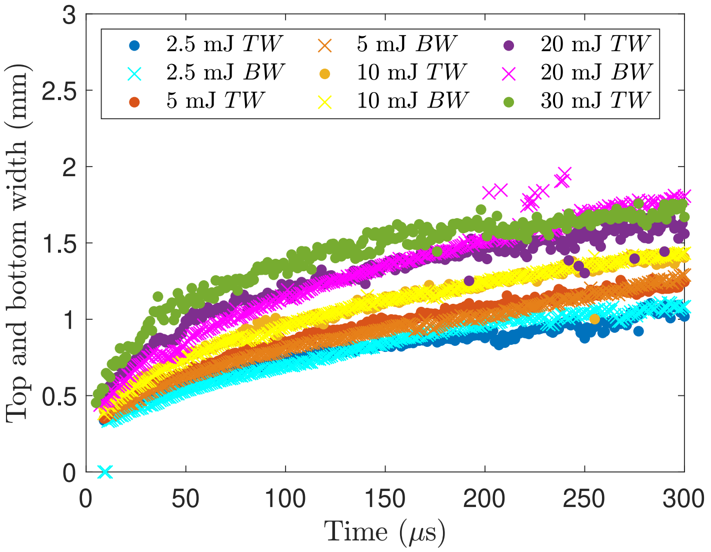

Figure 8.4: Crown width over time after laser impact on liquid tin, using different laser energies. Short laser pulses of 8 ns are focused to an 66 μm FWHM Gaussian spot. The top width (TW) and bottom width (BW) are both plotted, good agreement is found.

During crown formation a swell wave is created on the outside of the crown, best shown in figure 7.5b. The purple line shows the height of the surface of the film, however, 300 μs after high energy laser impact this surface is not visible anymore. One can imagine that the definition of the height we choose to measure the crown bottom width matters greatly. Choosing this height close to the purple line, results in the bottom width being a multiple of the top width. Moving up and it becomes comparable to the top width. We used a standard offset of 30 pixels from the purple line, seen in figure 8.5 in light blue, to create figure 8.4. However, this resulted in the bottom crown of the 30 mJ measurement to leave the measured region, because of the large swell wave. In figure 7.5b a moving boundary over time is used seen in red. Measurements obtained using this moving boundary method are not directly comparable to measurements using a constant offset. For that reason these measurements were left out of figure 8.4.

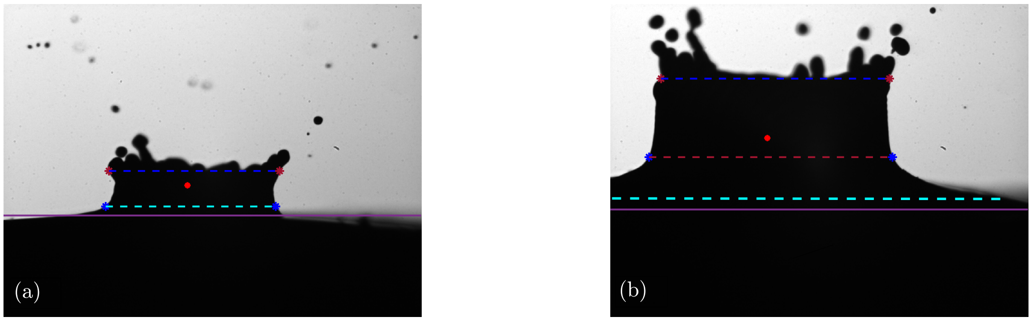

Figure 8.5: Image processing to find top (dark blue) and bottom width (cyan) for a 10 mJ laser pulse after 200 μs (a) and a 30 mJ laser pulse after 300 μs. (b) The height on which the bottom crown is measured is a problem because of the swell wave on the outside of the crown. A moving bottom is used to find the bottom width seen in red.

8.5 Data processing software

In this section a more in depth explanation of the defined Region of Interest (RoI) is given and the full Matlab code is provided. The RoI is define in line 92 of the matlab code. What it effectively does is using the two most extreme values in the x direction along the previously determined top-half boundary of the crown seen in red in figure 8.6, and measure the distance between these two values. Then all values laying in the outer 20% of the boundary are excluded. This is done because the top half of the crown also includes edges of the crown as seen in figure 8.6 in blue. These have to be excluded otherwise these values interfere with finding the lowest value on the rim. The excluded outer percentage is chosen such that the edges are excluded for all measured data in a robust manner. This way the value (20%) does not have to be optimized every measurement. In addition, in later time steps when the crown starts to collapse the shape of the crown will be rounded, seen in figure 4.1i, here the outer parts of the crown are also subtracted using this mechanism to get a more accurate rim detection. The the Note that lowest point along the RoI is detected as the rim height, as already mentioned in Section 3.2.

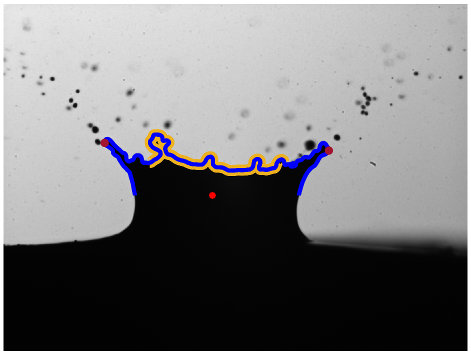

Figure 8.6: Crown 100 μs after 20 mJ laser impact on liquid tin. The most extreme values in the x direction are indicated in red. The center of mass is also shown in red. The top half boundary of the crown is seen in blue. The selected region of interest is seen in yellow.

The code to analyse and extract the measured variables is provided below, in green comments to explain operations done are added.

```matlab
% clc
% clear variables
% close all
 clear all
%% List of variables to vary
 binaryThreshold = 165;   %165   % Grayvalue threshold for binarization. Use ... binaryThreshold = 0 for automatic multithresholding.
 areaThreshold = 4000;       % Pixel x pixel value threshold for small object ... filtering.
 pixelValue = 2.7;           % Scale of each pixel in microns.
 NrepeatedMeasurements = 1; % Number of measurements on the same time step.

%Find location of files on PC
folder='C:\Users\s132290\Desktop\Afstuderen\DATA\11122019\ ...'


tiffFiles = dir([folder filesep '*camera1*']);   %name and number al files
numfiles = length(tiffFiles); %extract amount of files
mydata = cell(1, numfiles); %create cell for lower running time

% Import background image for subtraction.
BG = imread(fullfile(folder,tiffFiles(2).name));
%% Choosing bottom of film manually
 figure
 imshow(BG) %plot background

 lijn=682; %manually picked bottom position based on background image
 start=5 ;%first file on which splash is large enough to be detected
 IBG = 255 - BG;                    % invert background.

% Extract filename for display in figures
fullFileName = tiffFiles(3).name;           % Arbitrary filename, all relevant ... info in all filenames
fileName = folder(:,(92:100))       % Select relevant section of the filename, ... including: date+time, energy, spotsize, timesteps, location and delay.
time=1:1:numfiles;
     y=zeros(1,4);
     for l = NrepeatedMeasurements+start:1:numfiles; % for loop over all files
      w(l)=l %counter
      mydata{l} = imread(fullfile(folder,tiffFiles(l).name));  % Read in image.
      invertedImage = 255 - mydata{l};
%% Subtract background from image and increase contrast.
    diff = invertedImage - IBG;
    TotalGreyscale=sum(diff,'all'); %Find sum of greyscale values
%     contrastDiff = diff; %Sometimes no contrast necessary, then use this
    contrastDiff = imadjust(diff); %enhance contrast by moving center values ... greyscale histogram to the extremes
%     figure
%     imshow(invertedImage)
    if binaryThreshold == 0
        binaryThreshold = multithresh(contrastDiff); %automatic multitreshing ... can be used, if threshold is set to 0
    end
    % Binarise image using threshold and convert to logical array.
    binaryImage = diff > binaryThreshold; %smaller than threshold=0
    labeledImage = logical(binaryImage); %create binary image
    % Set function for integer recognition.
    isaninteger = @(x) mod(x, 1) == 0;
Totalbinary=sum(labeledImage,'all'); %sum all binary values
%     figure
```

```
%     imshow(labeledImage)

    % Remove small objects < 'areaThreshold' pixels.
    binaryImage = bwareaopen(binaryImage,areaThreshold);

%     figure
%     imshow(binaryImage)
    measurement = regionprops(binaryImage,'Centroid');
    centroids = [measurement.Centroid]; %Find center of splash by finding the ...
        center of 'mass' (average value in x and y)

    %save all images in workspace
    mydata_threshold{l} = binaryImage;

%% Find origin of splash
    col = round(centroids(1)); % low part of the figure; Col for up-down crown ...
        and row for left and right crown
%% Boundary tracking
    row = find(mydata_threshold{l}(:,col),1,'last'); % find the coordinate of ...
        the first non-zero point in the origin column
    boundary = bwtraceboundary(mydata_threshold{l}, [row, col], 'W'); %% Track ...
        boundary from binaryimage starting with position [row,col]
          %fast plot figure boundary
          %figure
          %plot(boundary(:,2), boundary(:,1),'color',[0,0,0]+0.5); hold on;
%% extract relevant variables
  %extreme height and width in pixels
        Crown_height1(l) = max(boundary(:,1))-min(boundary(:,1));
        Crown_width1(l)=max(boundary(:,2))-min(boundary(:,2));

y1=find(boundary(:,1)>centroids(2)); %select top part of upsidedown splash
y2=find(boundary(:,1)<centroids(2)); %select bottom part of upsidedown splash
y3=find(boundary(:,2)>centroids(1));%select right part of upsidedown splash
y4=find(boundary(:,2)<centroids(1)); %select left part of upsidedown splash

%Compute top boundary
topboundary=boundary(y2,:);
        Crown_widthtopmax(l)=max(boundary(y2,2))-min(boundary(y2,2));

%Find points which lay at  the rim 20% of the points of both sides is
%excluded to be certain only top is found and not also sides
RoItop=find(topboundary(:,2)>(min(topboundary(:,2))+0.2.*Crown_widthtopmax(l)) ...
    & topboundary(:,2)<(max(topboundary(:,2))-0.2.*Crown_widthtopmax(l)) & ...
    topboundary(:,1)<centroids(2));
RoIbottom=find(boundary(:,2)>(min(boundary(:,2))+0.2.*Crown_width1(l)) & ...
    boundary(:,2)<(max(boundary(:,2))-0.2.*Crown_width1(l)) & ...
    boundary(:,1)>centroids(2));

%Find top rim even a bit narrower and see if that matters
RoItopnarrow=find(topboundary(:,2)>(min(topboundary(:,2))+0.25.*Crown_widthtopmax(l)) ...
    & topboundary(:,2)<(max(topboundary(:,2))-0.25.*Crown_widthtopmax(l)) & ...
    topboundary(:,1)<centroids(2));
% ...
    testlinks=find(topboundary(:,2)>(min(topboundary(:,2))+0.15.*Crown_widthtopmax(l)))
% ...
    testrechts=find(topboundary(:,2)<(max(topboundary(:,2))-0.15.*Crown_widthtopmax(l)))

%average bottomofcrown see if it converges
bottomposition(l)=mean(boundary(RoIbottom,1));

%calculate the height position in pixels in different ways
Rimheightmin(l)=max(topboundary(RoItopnarrow,1)); %find minimum height in ...
    region of interest
Rimheightaverage(l)=mean(topboundary(RoItop,1)); %Find average height over ...
```

```
    region of interest
Jetheight(l)=min(topboundary(RoItop,1)); %Find max height over region of interest

%Findlocations where average rim height crosses crown.
topcrossing=find(topboundary(:,1)==round(Rimheightaverage(l)));
RTW=max(topboundary(topcrossing,2)); %rightposition
LTW=min(topboundary(topcrossing,2)); %leftposition
TopWidth(l)=pixelValue*(RTW-LTW); %Topwidth coming from average

%Findlocations where min rim height crosses crown.
topcrossingmin=find(topboundary(:,1)==round(Rimheightmin(l)));
RTWmin=max(topboundary(topcrossingmin,2)); %rightposition
LTWmin=min(topboundary(topcrossingmin,2)); %leftposition
TopWidthmin(l)=pixelValue*(RTWmin-LTWmin); %Topwidth coming from min value

botcrossing=find(boundary(:,1)==lijn-10); %Use manually picked bottom position ...
    to find bottom crown width
RBWmin=max(boundary(botcrossing,2)); %right bottom
LBWmin=min(boundary(botcrossing,2)); %left bottom
BotWidthmin(l)=pixelValue*(RBWmin-LBWmin); %bottom width
end

%nonmanually picked bottom position
Averagebottomposition=mean(nonzeros(bottomposition))

%calculate the height in pixels in different ways using min, average, and
%max
Rimheightminabs=pixelValue*(lijn-Rimheightmin(1:numfiles));
Rimheightaverageabs=pixelValue*(lijn-Rimheightaverage(1:numfiles));
Jetheightabs=pixelValue*(lijn-Jetheight(1:numfiles));
%set not measureable frames to 0 instead to =lijn
Rimheightminabs(1:start)=0;
Rimheightaverageabs(1:start)=0;
Jetheightabs(1:start)=0;
 %% save matlab file with outputs and txt files with outputs
 save(fileName,'Rimheightminabs','Rimheightaverageabs','Jetheightabs',...
     'TopWidthmin','TopWidth','BotWidthmin','time')
% %TopWidth=transpose(TopWidth);
TxtOutput=transpose([Rimheightminabs; Rimheightaverageabs; Jetheightabs;...
    TopWidthmin; TopWidth; BotWidthmin; time]);

writematrix(TxtOutput,fileName) ;
```

8.6 Uncertainty analysis

Uncertainties of individual measurements are treated with 100% confident intervals based on inherent experimental uncertainties. For example, uncertainties in figure 4.4 are calculated using the following method:

$$\Delta y = \Sigma\big(\Delta x_i \frac{\partial y}{\partial x_i}\big), \tag{8.1}$$

with y the dependent variable and x_i the different independent variables.

Uncertainties corresponding to fitting parameters are evaluated as standard deviations.